



CHALMERS
UNIVERSITY OF TECHNOLOGY

Corrosion of zirconium fuel cladding inside a boiling water reactor: A post-irradiation study by atom probe tomography

Downloaded from: <https://research.chalmers.se>, 2025-05-12 02:51 UTC

Citation for the original published paper (version of record):

Mayweg, D., Eriksson Limminger, J., Sattari, M. et al (2025). Corrosion of zirconium fuel cladding inside a boiling water reactor: A post-irradiation study by atom probe tomography. *Acta Materialia*, 292. <http://dx.doi.org/10.1016/j.actamat.2025.121020>

N.B. When citing this work, cite the original published paper.



Corrosion of zirconium fuel cladding inside a boiling water reactor: A post-irradiation study by atom probe tomography

David Mayweg^{a,*}, Johan Eriksson^{a,b}, Mohammad Sattari^a, Hans-Olof Andrén^a,
Mattias Thuvander^a

^a Department of Physics, Chalmers University of Technology, Göteborg SE-412 96, Sweden

^b Department of Chemistry and Chemical Engineering, Chalmers University of Technology, Göteborg SE-412 96, Sweden

ARTICLE INFO

Keywords:

Zr fuel cladding
Corrosion
Atom probe tomography
Radiation damage

ABSTRACT

The life-time-limiting factors of zirconium-based fuel cladding in water-cooled and -moderated nuclear power reactors are corrosion and associated hydrogen pickup. Corrosion performance in reactor is significantly worse in comparison to autoclave exposure. The accelerated degradation becomes particularly severe with the accumulation of radiation damage that is caused by fast neutrons. This work aims to expand the understanding of the underlying mechanisms governing the in-reactor corrosion process by nano-scale characterization of high-burnup fuel cladding tubes from operation in the boiling water reactor Oskarshamn 3 mainly by atom probe tomography. We present data from the oxide and the oxide-metal interface and point out the differences with the comparatively well-known behaviour in autoclave corrosion tests. The main aspect is the interaction between alloying elements, irradiation-induced defects and zirconium oxidation: Irradiation-induced FeCrNi clusters seem to slightly accelerate the diffusion of oxygen within the basal plane of the hexagonal metal matrix and dissolve in the oxygen-saturated zirconium metal that develops before zirconia formation takes place, and c-component dislocation loops, characteristic of high damage levels, might offer enhanced oxide nucleation sites that potentially explain the rapid degradation observed after some years of reactor operation. In addition, pores can be construed as a potential pathway for accelerated hydrogen pickup, similar to processes postulated in the literature. The results in this study give some novel insights into the mechanisms of in-reactor degradation of zirconium-based alloys and highlight the necessity to characterize materials from actual reactor operation.

1. Introduction

In nuclear power reactors zirconium alloys are used as cladding tubes that contain the nuclear fuel. They thus constitute the barrier between the fuel and the cooling water. During reactor operation, cladding tubes are affected by three major degradation mechanisms, namely, irradiation damage from fast neutrons, hydrogen pickup (HPU) and water-side corrosion. While Zr has a small capture cross section for thermal neutrons and is therefore beneficial for neutron economy, in its pure form it does not have sufficient mechanical strength nor corrosion performance for cladding applications in water-cooled and -moderated reactors. Therefore, the following alloying elements are added to improve the performance: Sn and O to improve mechanical properties [1]; Fe, Cr and Ni to improve the corrosion resistance of, e.g., Zr-Sn alloys [1]; Nb to significantly improve resistance to corrosion and HPU [2]. Sn and O are in solid solution, while Fe, Cr and Ni have a low solubility in α -Zr and

form intermetallic precipitates often referred to as *secondary phase particles* (SPPs) [3,4] (the most relevant for the present work are $Zr(Fe,Cr)_2$ and $Zr_2(Fe,Ni)$).

The corrosion behaviour of Zr-based fuel cladding depends on the corrosive environment as well as composition and microstructure of the cladding material [1]. The protective oxide, zirconia (ZrO_2), is an n-type semiconductor [5], is inward-growing and has a Pilling-Bedworth ratio (volume of oxide to volume of metal) of ~ 1.56 [6]. This leads to large compressive/tensile stresses in the oxide/metal, causing plastic deformation forming (sub)grains in the metal close to the interface [7]. The rate-controlling process in the Wagnerian oxide scale growth is either O transport across the scale to the oxide-metal interface or outward electron transport [8]. In pressurized water reactors (PWRs) (where no steam is present) the main concern is the velocity of uniform corrosion. Historically, Zircaloy-4 (alloyed with Sn, O, Fe, and Cr) was mainly used in western PWRs whereas Russian designs used Zr-1 %Nb (E110). To

* Corresponding author.

E-mail addresses: david.mayweg@chalmers.se, david.mayweg@gmail.com (D. Mayweg).

<https://doi.org/10.1016/j.actamat.2025.121020>

Received 2 September 2024; Received in revised form 13 March 2025; Accepted 4 April 2025

Available online 5 April 2025

1359-6454/© 2025 The Authors. Published by Elsevier Inc. on behalf of Acta Materialia Inc. This is an open access article under the CC BY license (<http://creativecommons.org/licenses/by/4.0/>).

date, Zircaloy-4 has largely been replaced by Zr-Nb alloys such as M5™, ZIRLO® and AXIOM® that have lower HPU and improved corrosion performance. Nb-containing alloys do, however, not perform well in the more aggressive environments of boiling water reactors (BWRs) [9]. Therefore, Zircaloy-2 (alloyed with Sn, O, Fe, Cr and Ni) has been used for many decades. In BWRs localized or ‘nodular’ corrosion was a prominent issue, but it has largely been resolved by optimizing the size and distribution of SPPs [10–12] such that nodular corrosion is avoided at the cost of a slightly increased uniform corrosion. The corrosion performance of the relatively newly developed alloys GNF-Ziron and HiFi™ is further improved. Both alloys contain increased amounts of Fe (higher than the Zircaloy-2 standard) that is mainly added to lower HPU [13,14].

Performance of corrosion is usually rated based on autoclave experiments because they are more accessible and less expensive than in-reactor testing. Autoclave exposures are designed to emulate the reactor conditions as closely as possible, which means that the water chemistry is intended to mimic that found in reactor. For example, oxygenated water is used to account for radiolysis taking place during reactor operation. Importantly, the actual in-reactor performance is significantly worse, i.e., the oxide scale thickness is much larger than that estimated from autoclave experiments [15,16]. Therefore, autoclave-based rating, while a useful tool, has its limitations [17]. Due to the difficulties associated with handling radioactive materials, the majority of investigations of Zr alloy corrosion and HPU have been and will be performed with autoclave-tested materials, although the effect of irradiation is missing and higher temperatures typically are used to reduce the time of exposure.

In the early stage of oxidation (called *pre-transition*), the oxide growth rate is sub-parabolic (sometimes also referred to as cubic [8,18]) and the oxide morphology is homogeneous and little porosity is present [19,20]. In this pre-transition regime the oxidation rate does not significantly differ between autoclave and reactor (it is largely independent of the neutron fluence) and is active up to a scale thickness of approximately 2 μm [16].

In pre-transition autoclave-corroded fuel cladding materials a sub-oxide (hexagonal structure of composition ZrO [21–24]) has been described to be present between the ZrO₂ and the metal [21,25–32]. Its thickness has been observed to vary significantly along the interface [21]. Such suboxides have been characterized by energy-dispersive x-ray spectroscopy (EDS) [33] and electron energy loss spectroscopy (EELS) [25,26,30], diffraction [34] and atom probe tomography (APT) [29–31,35]. Below the suboxide, O-saturated Zr metal with ~ 29 at. % O is present (showing up as a plateau in concentration profiles), which is followed by a region with a smooth transition of O until the bulk concentration is reached. In the post-transition regime (discussed below) generally no suboxide is present in autoclave-corroded material [21].

The *post-transition* regime is marked by cyclic behaviour and acceleration of the corrosion process: repassivation occurs after breakdowns in the protective properties of the oxide scale of approximately 2 μm thickness [36,37]. This takes place continuously and in later stages it is often approximated as linear growth [8,38,39] (possibly with more than one stage [38]) and is sometimes also referred to as *breakaway* corrosion [18,40,41]. In autoclave the cyclic behaviour of oxide growth is often associated with formation of columnar oxide grains at the oxide-metal interface [42]. These grow to a thickness of approximately 2 μm before they become unstable due to compressive stresses [8] and a layer of equiaxed grains forms at the interface. Below the layer of equiaxed grains a new layer of columnar grains starts to form, and the cycle continues in this manner [43]. The in-reactor oxide morphology differs from autoclave-formed oxide and has much less well-defined columnar grains [34].

The key motivation for the present work is that in the *post-transition* regime, corrosion is strongly accelerated in reactor compared to autoclave [15,16]; the end-of-life oxide scale thickness can be more than 40 times thicker than estimated from autoclave [16]. There appears to be a

certain time for corrosion to accelerate in reactor [16] and this acceleration shows dependence on the temperature and the damage level [16, 44], in which higher flux leads to a higher corrosion rate [15,16].

Diffusion through the scale is likely not significantly increased by irradiation-induced atomic-scale defects inside the oxide [8]. Notwithstanding this, it has been proposed that a contribution to the increase in corrosion rate could be due to intergranular porosity [34], which is certainly reasonable since it will lead to an increase in the transport of O (and H) across the oxide scale. Most relevant, however, is the transport across the innermost oxide, the ‘*barrier layer*’ [45] and the formation of zirconia at the oxide-metal interface. The barrier layer has been demonstrated to be the protective (or active) layer during autoclave corrosion [36,46]. In reactor the barrier layer potentially becomes thinner at higher burnup [47]. The oxide-metal interface has been reported to be undulated after autoclave [33,48] as well as reactor exposure [34,49,50]. While processes in the oxide and at the oxide-metal interface are likely in some way (even indirectly) affected by irradiation, accelerated corrosion was also found in specimens that were repolished after reaching the post-transition regime [16]. It is therefore reasonable to assume that this acceleration is at least in part caused by the accumulated irradiation damage in the base metal. In order to fundamentally understand this process, one needs to connect microstructural observations in the metal as well as in the oxide close to the metal-oxide interface to derive potential mechanisms that elucidate the observed macroscopic behaviour.

One important difference between corrosion in autoclave and reactor is that during reactor operation the SPPs dissolve to a large extent due to irradiation, releasing Fe, Cr and Ni into the Zr metal matrix where segregation to irradiation-induced defects (mostly a-loops) [51–60] takes place. The distribution of the transition metals potentially plays a significant role in determining the corrosion characteristics [61]. The release of Fe from Zr(Fe,Cr)₂-SPPs takes place preferentially, while Cr remains in the now amorphous particles, which are only fully dissolved at high fluences. It has been reported that corrosion is significantly accelerated once SPPs have (almost) fully dissolved [62]. Unsurprisingly, segregation of the said elements to grain boundaries (GBs) is found, both before and after reactor operation [50,54,58,63,64]. SPPs and GBs have been shown to be incorporated into the oxide after autoclave [65] and reactor exposure [16,66]. The alloying element distribution in the oxide of reactor-exposed Zr alloys is of interest to study, as it is believed to affect the corrosion and HPU behaviour. A mechanistic description of the oxidation process [67], which is supported by density functional theory (DFT) calculations, proposes that the presence of Fe and Ni and their ratio at oxide GBs are important for HPU [68,69].

Due to its combination of high mass resolution and sub-nm spatial resolution APT is a technique well suited for analysing the distribution of low-concentration alloying elements at the near-atomic scale [70]. APT has been employed to characterize Zr alloys in the past, e.g., hydride formation [35,71–73] and clustering of alloying elements at irradiation-induced defects [53,54,57,58,74]. Zr corrosion has also been investigated in cladding materials from autoclave testing [29,35] and PWR operation [64], but so far a thorough APT investigation of the oxide-metal interface has been lacking.

In this work we present extensive data from APT analyses of the oxide and the oxide-metal interface from high-burnup cladding tubes after service in a commercial BWR. We investigated samples from two cladding tubes, one manufactured from *Zircaloy-2* and one from a similar model alloy, which we designate as ‘*Zircaloy-2 Fe+*’ that has higher Fe and Cr contents, which reduces HPU. Since the damage to the matrix (and possibly the disappearance of SPPs) is one important aspect related to accelerated in-reactor corrosion, it is necessary to understand the mechanism(s) taking place at the oxide-metal interface, because – irrespective of the O transport across the oxide scale – in some manner this damage leads to an acceleration of the oxide growth into the metal (as well as increasing HPU).

2. Materials and methods

2.1. Specimen information

We investigated two fuel cladding tubes after 2082 days of reactor operation in the BWR Oskarshamn 3 with designations O3E9 (Zircaloy-2) and O3F9 (Zircaloy-2 Fe+, which has an increased content of Fe and Cr higher than the ASTM specifications of Zircaloy-2 [75] to reduce the HPU [76]; it is similar to HiFi and is referred to as “Alloy 2” in Ref. [77]). Both materials were produced by Sandvik Materials Technology AB (now Alleima AB) using the heat treatment scheme LK3 [10]. The fuel assemblies were produced by Westinghouse Electric Sweden AB. The compositions in the as-produced condition are given in Table 1.

We have previously published investigations performed on the same samples that focused on clustering in the metal, hydrogen analysis and formation of pure Zr islands inside c-loops (see [56,77–79]). Relevant information about the irradiation conditions and post-irradiation investigations can be found in Table 2. Based on comparison with, e.g., [16], the cladding tubes are in a regime where accelerated corrosion is expected.

2.2. Atom probe tomography

2.2.1. Specimen preparation and experiments

Preparation of needle-shaped APT specimens was performed via standard lift-out methods [82] (final annular milling at 30 kV and 30–50 pA with an inner diameter of the mask of 100–150 nm, low-kV cleaning to remove some surface damage for 30–60 s at 5 and 2 kV and 45 and 28 pA) using dual-beam FIB-SEM instruments (FEI Versa3D and Tescan GAIA3, the latter equipped with a Leica VCT 500 cryo-stage). Lift-outs were mostly made with the oxide-metal interface aligned perpendicular to the APT specimen axis. Five APT specimens from each cladding tube were prepared with the metal-oxide interface parallel to the specimen axis.

For 19 specimens the annular milling was conducted at a temperature below –150 °C. Such a procedure intends to prevent the transformation of α -Zr into δ -, or γ -hydride, which is well-known to take place in metals and alloys with high affinity for H when specimens are very thin [83,84]. While this is a necessary step if the analysis of dislocations by TEM is intended or the H signal is of interest, we have recently shown that a transformation into δ -hydride does not lead to a change in the distribution of other elements like solute clustering at dislocation loops [77]. Here it was used in order to try to obtain data of hydrides at or near the oxide-metal interface. However, only one single of these specimens captured the oxide-metal interface and no hydride volumes were encountered. An overview of the specimens prepared is given in Table 3.

APT was performed using an Imago LEAP 3000X HR (green laser, 535 nm wavelength), and a Cameca LEAP 6000 XR (UV laser, 257.5 nm wavelength). The base temperature was set between 50 K and 70 K. Laser pulse energies (LPEs) used were 250–400 pJ in the LEAP 3000X HR and 50–150 pJ in the LEAP 6000 XR. Higher LPEs (>100 pJ) that result in higher surface temperatures, and thus field evaporation at relatively lower standing voltages, were used on the oxide to reduce the load on the specimens and thus decrease the risk of specimen fracture. Once the oxide had been passed, we usually lowered the LPE to increase the field magnitude at which evaporation occurs so Fe, Ni and Cr are detected as doubly charged ions, thus avoiding overlaps with other species. Still, in

Table 1

Chemical composition of the investigated fuel cladding tubes (balance Zr).

Alloy		Fe	Cr	Ni	Sn	O	C	Si	N	Al
Zircaloy-2	(at%/at ppm)	0.29	0.23	0.094	1.14	0.68	/	1100	290	260
	(wt%/wt ppm)	0.18	0.13	0.061	1.49	0.12	/	143	91	<30
Zircaloy-2 Fe+	(at%/at ppm)	0.58	0.31	0.097	1.00	0.68	/	900	290	250
	(wt%/wt ppm)	0.36	0.18	0.063	1.31	0.12	/	120	90	38

Table 2

Specimen information.

Alloy	Zircaloy-2	Zircaloy-2 Fe+
Heat treatment code	Westinghouse LK3 [10]	
Irradiation time (d)	2082	2082
Coolant saturation temperature (°C)	284	284
Rod average burnup, calculated (MWd/kgU)	52	52
Burnup, average, measured (MWd/kgU) [80]	Not measured	56, lower half
Position in fuel assembly	E9	F9
Elevation from rod bottom (mm)	2642–2645	2666–2669
Fast neutron fluence ($n\ m^{-2}$)	1.2×10^{26}	1.2×10^{26}
Damage level (dpa) [81]	19	19
Oxide thickness (μm) from FIB cross sections	12.2 ± 1.3	9.8 ± 0.6
Oxide thickness (μm), measured at 0/90/180/270° on metallographic cross sections	7, 9, 11, 22	11, 10, 10, 11
Rod growth (%)	0.34	0.38
Hydrogen concentration post-irradiation (wt ppm)	200 ± 29	134 ± 9

laser pulsing only a small fraction of Ni is detected at 29 Da, meaning that most Ni is lost due to peak overlap between Ni^+ and Sn^{++} . Reconstructions were made choosing only smooth parts of the voltage curves. Reconstructions and analyses were carried out in IVAS 3.6.14 and AP Suite 6.3 with a voxel size of $1 \times 1 \times 1$ nm and a delocalization of $1.5 \times 3 \times 3$ nm and the built-in isoconcentration surface (ICS) tool was used for visual analysis and creating proximity histograms (‘proxigrams’ [85]). Ranging was performed individually for each dataset or sub-volume of interest. Compositions were quantified using the built-in algorithm in AP Suite. Hydrogen was always excluded, since hydridation by FIB-milling [73,83] often occurs and, especially in laser measurements, the hydrogen distribution is inhomogeneous across the specimen volume with a (unphysically high) maximum hydrogen fraction on the opposite side of the laser illumination. In some instances, it can be useful to have a measure of local field variations, which can be obtained from the charge state ratio (CSR), which in the case of the here analysed material is defined by the ratio of Zr^{+++} to Zr^+ ions. This is based on the probability of reaching a higher charge state by post-evaporation ionization in higher relative fields [86].

The supplementary material includes a section about some of the relevant APT-related artefacts. Here only one important issue specific to the analysis of oxide-metal interfaces is expounded upon:

2.2.1.1. Presence of a layer with suboxide stoichiometry (ZrO) between zirconia (ZrO_2) and O-rich metal Zr(O). One specific artefact that is relevant in the context of APT investigations targeting Zr corrosion is the presence of an additional O-rich/oxide layer in APT datasets, which is dependent on the analysis sequence: if ZrO_2 is at the apex of a specimen and the metal below, an additional layer of distinct composition (Zr:O = 50:50) has been observed. Such is not the case when the analysis direction is reversed from the metal into the oxide [87]. This is attributed to migration of O^{2-} from the oxide into the metal below under the influence of the strong electric field.

The presence of a hexagonal suboxide (with Zr:O = 50:50) of up to several 100 nm thickness in the case of pre-transition oxide scales is well known. In APT measurements in previous work this phase was distinguished from ZrO_2 by the absence of O_2^+ -ions, which are used as markers for the presence of the oxide [29]. The existence (and presence) of such a suboxide has also been confirmed by techniques other than APT,

Table 3

Overview of prepared APT specimens and conducted experiments. Of a total of 55 prepared specimens targeting the oxide-metal (O/M) interface, 5 APT measurements captured this region. Specimen axis oriented along the direction perpendicular to the oxide-metal interface means the same as radial direction with respect to the cladding tube directions (see inset in Fig. 2).

Alloy	Lift-out direction with respect to O/M interface	Annular milling temperature	No. of specimens prepared	No. of successful O/M datasets (10 ⁶ detected ions)	No. of successful oxide datasets (10 ⁶ detected ions)
Zircaloy-2	Perpendicular	RT	20	none	1 (3)
	Parallel	- 150°C	10	1 (8)	none
Zircaloy-2 Fe+	Parallel	RT	5	3 (32, 17, 0.8)	none
	Perpendicular	RT	6	1 (14)	2 (5, 9)
	Perpendicular	- 150°C	9	none	1 (2)
	Parallel	RT	5	1 (2)	1 (3)

namely, EELS [26,48] and electron diffraction [26,48,88]. There is hence no reasonable doubt that this phase can be found, the question becomes rather whether a specific feature with a thickness of a few (ten) nm and composition ZrO found in APT is real or an artefact.

Fig. 1 shows a comparison of segments of oxide-metal interfaces where in (a) the oxide lies above the metal and vice versa in (b) (the full reconstructions are shown in Figs. S5 (a) and S1). In both cases the lift-out was performed with the specimen axis aligned with the axial direction of the tube, i.e., macroscopically parallel to the oxide-metal interface. Both specimens were measured under similar conditions (100 pJ, 70 K, 0.2 % target detection rate) in the same instrument. Comparing the ion maps in Fig. 1(a) and (b) it is obvious that above the interface (here defined as 50 at% Zr ICS) the distribution of the O-containing (molecular) ions is not homogenous in (a), especially O₂⁺, O⁺, ZrO₂^{+/++} and Zr₂O₃^{+/++}, while it is in (b), although the shape of the interface is more complex there. These differences are reflected in the proxigrams, which show an extended transition region in (c) vs. a smooth apparent compositional change in (e) as is typical for phase boundaries captured by APT (see, e.g., [89–91]). The differences are further highlighted in the proxigrams of the ionic fractions depicted in (d) and (f). While the O-containing ionic species exhibit different profiles in the ‘oxide-to-metal’ dataset (d) they are all similarly monotonically decreasing in the ‘metal-to-oxide’ case (f). In light of this analysis, we conclude that – although a 5–15 nm thick layer of ZrO composition is found in many APT measurements of the oxide-metal interface – no suboxide is found in our data, rather these features are APT artefacts.

2.3. Electron microscopy

SEM images were captured with the *Versa3D* also used for FIB-based specimen preparation for APT and TEM. TEM analyses were performed using an *FEI Titan 80-300* at 300 kV. A high-angle annular dark-field (HAADF) detector was used to highlight the location and morphology of the oxide-metal interface. EDS data were analysed by standardless quantification using the Cliff-Lorimer method. The input value for the lamella thickness in the software was incrementally changed until the known O concentration of the oxide (66.7 at%) was obtained. The calculated thickness was then used to quantify the composition of the adjacent metal regions.

3. Results

3.1. Electron microscopy

Fig. 2(a) provides an overview of a sample from a cladding tube viewed in the radial direction. As illustrated in the inset (upper right), the tube segment has a chamfer that was ground in order to expose the metal-oxide interface and enable simplified preparation for TEM and APT by FIB. Fig. 2(b) shows a FIB cross section of the oxide-metal interface (here viewed in the axial direction), where hydrides and SPPs are visible in the metal. The oxide scale exhibits tangential

cracking. The cracks that are opened the widest are almost continuously connected. We have also observed this in further cross sections although the distance between the wide, continuous cracks and the oxide-metal interface varied. Fig. 2(c) and (d) show specimens at an early stage of the annular milling performed to produce needles for APT analysis. The oxide-metal interfaces are aligned roughly perpendicular and parallel to the length axes in (c) and (d), respectively.

Fig. 3 depicts (S)TEM images of the oxide-metal interface from both alloys with view in the axial direction of the tubes (i.e., the cross sections/lamella planes are perpendicular to the oxide-metal interface. In (a) and (b) STEM-HAADF images of both investigated alloys show its serrated nature. Lower-brightness regions in the metal are lenticular hydrides, the smaller of which have likely been created by FIB-milling [83]. The higher brightness at the oxide-metal interface (more clearly seen in (a) than in (b)) is associated with higher O concentrations (maximum solubility of O in Zr is approximately 29 at% at relevant temperatures [92]). The measured O fraction in the metal near the interface (i.e., a few tens of nm away) ranges from approximately 20 to 30 at% and in one case approximately 50 at% (see Fig. 3 (a₂) and (b₂)). Dark-field images (Fig. 3 (a₃) and (b₃)) highlight some columnar grains, but most grains had somewhat irregular shapes. In addition, oxide grain sizes of only a few nm in diameter were found (b₄).

The oxide grain morphology is hard to ascertain and in general grains cannot be easily distinguished. Among irregular-shaped grains of several 100 nm diameter, we did find a few columnar grains (few 100 by few tens of nm) in the bulk of the oxide (i.e., away from the oxide-metal interface) as shown in Fig. 3. There were, however, also regions with very small grain sizes, smaller than 5 nm (Fig. 3 (b₄)). Cracks are present throughout the oxide scale with the exception of the direct vicinity of the oxide-metal interface region that appears to be largely crack-free within roughly a few 100 nm from the interface. The vast majority of cracks run in circumferential direction; one exception can be seen in Fig. 3(a), where some cracks have a component in the radial direction. Cracks differ in size and distribution across the oxide thickness. The widest cracks are often connected several tens of μm (Fig. 2(b)); most cracks, however, are shorter than 1 μm.

3.2. Atom probe tomography

The APT results are presented sequentially from outer to inner: oxide, oxide-metal interface and finally the metal underneath the oxide.

3.2.1. Oxide

Fig. 4 comprises APT data from *Zircaloy-2 Fe+* showing the Fe and Ni distribution in ZrO₂, in (a) and (c), and in the metal for comparison in (b). The oxide datasets are from locations at maximum a few hundred nm away from the oxide-metal interface, and it is therefore reasonable to assume that they capture the barrier layer of the oxide. The metal dataset (Fig. 4(b)) was taken from several μm below the interface and has been transformed into a hydride by FIB preparation at room temperature. Long thermal tails of the main ionic species (O⁺, O₂⁺, ZrO^{+/++}; see Fig. S2) prevent meaningful quantification for the oxide datasets.

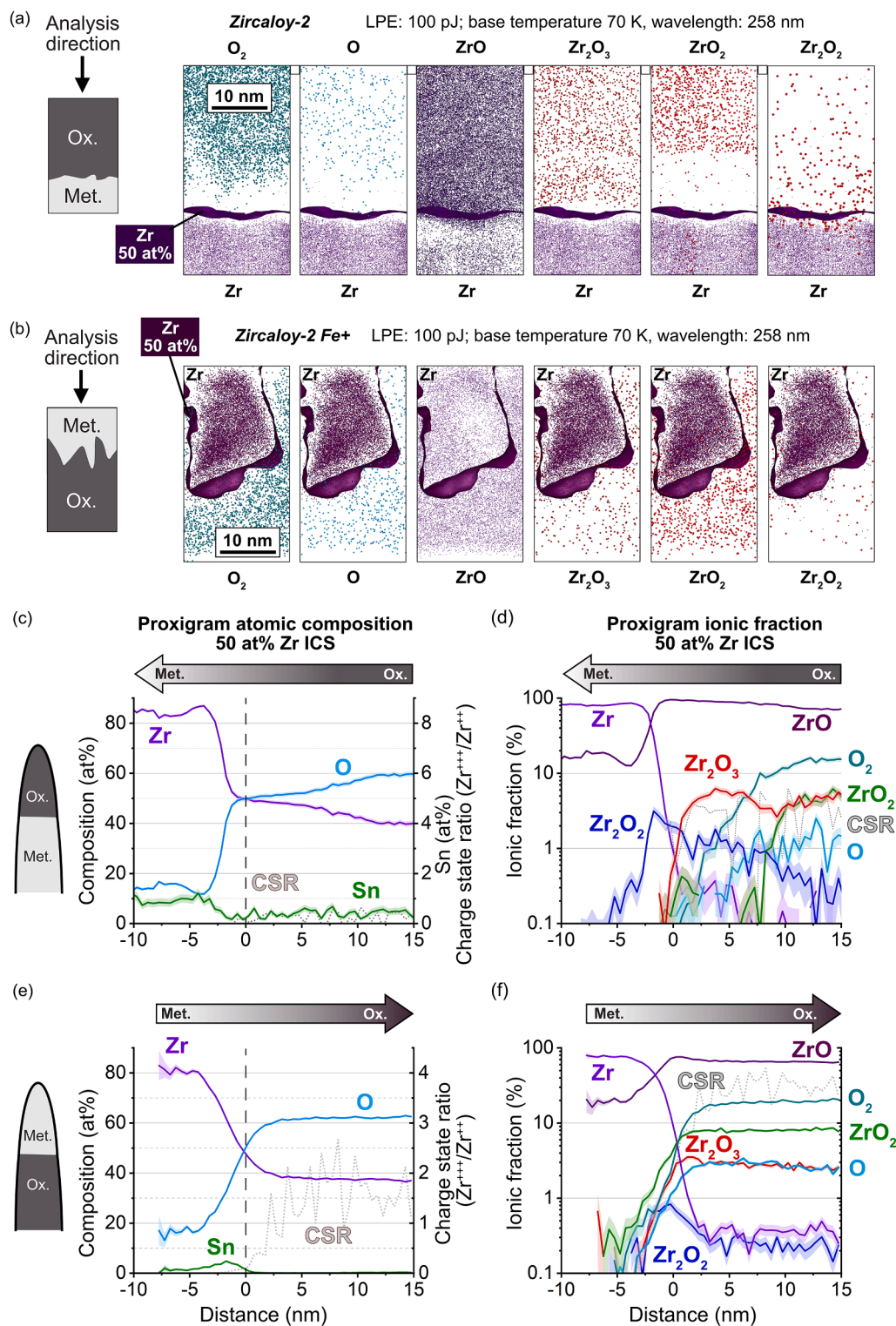


Fig. 1. Influence of APT analysis direction on the measured composition at the oxide-metal interface. If the oxide is at the specimen apex above the metal (see (a)) an additional ZrO layer appears that is absent if the metal is at the top above the oxide (see (b)). Proxigrams of atomic and ionic fractions of (a) and (b) are given in (c), (d) and (e), (f), respectively.

However, since the range between approximately 25 and 32 Da is not strongly affected by thermal tails, the distribution of Fe and Ni (Cr was not detected) can be assessed. It is immediately evident that clustering, which is clearly visible in the metal (Fig. 4(b)) is almost entirely absent in the oxide, which is an indication of cluster dissolution. This intuitive assessment is quantitatively confirmed by the comparison of the 1st

nearest neighbour (1NN) distributions of Fe and Ni in the datasets with that of a random mixture (a measure used to quantify non-random distribution of elements [93]) depicted in Fig. 4(e). While a significant difference between actual (dashed line) and random (solid line) distribution is evident in the metal, there is only a small difference for the distributions in the oxide.

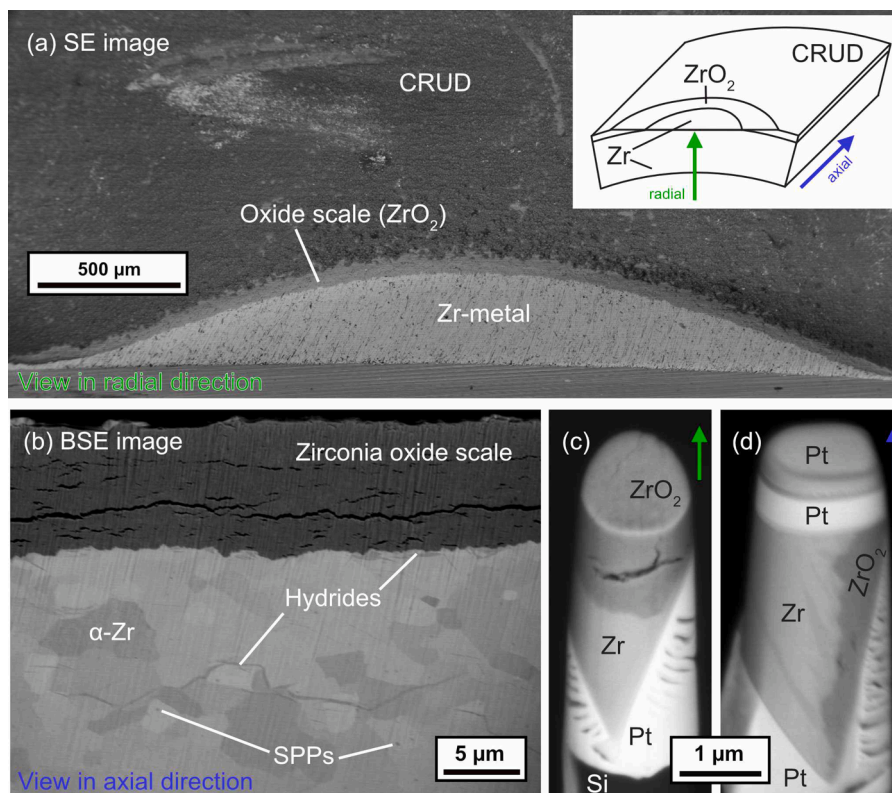


Fig. 2. (a) Secondary-electron (SE) image of the outer surface of a small section of a defueled cladding tube sample (Zircaloy-2), viewed in radial direction. (b) Back-scattered electron (BSE) image of the oxide-metal interface, viewed in axial direction. Cracks in the oxide are clearly visible, and in the bulk α -Zr metal, hydrides and SPPs can be seen. (c) and (d) are BSE images showing an intermediate step from annular milling in the preparation of APT specimens with (c) perpendicular and (d) parallel oxide-metal interface. The radial and axial cladding tube directions are indicated by green and blue arrows, respectively.

3.2.2. Metal-rich islands and pores within the oxide

Fig. 5 depicts a further oxide dataset, which only captures ZrO_2 but contains volumes enriched in Sn, Si and elements found in SPPs (Fe, Ni, Cr), as shown in Fig. 5(a) and such with increased Zr fractions (compared to ZrO_2) shown in (b). Several volumes show very high ionic densities (more than 10 times the average density, see Fig. 5(b) and (c)), which points to the presence of small pores (black arrows, see discussion of pores in ZrO_2 in [20]) or larger (low-field) metal islands (blue arrow). In the latter case, preferred evaporation due to the lower field causing trajectory aberrations takes place and causes higher densities in the reconstruction [94]. The significantly higher atomic Zr fraction (compared to ZrO_2) and the detection as ionic $Zr^{++/+}$ indicate that, locally, Zr is likely present in a metallic state. Fig. 5(d) depicts atom maps of Sn and Zr that show them aligned like pearls on a string, which is a typical behaviour when the evaporation sequence is not governed solely by the atomic structure but is severely disturbed by other factors. Note that the unphysically high density shown in the map is overlapping with the region of increased Sn and Zr fractions (the size is also unphysical because, in addition to the trajectory aberrations, it is influenced by reconstruction parameters and the choice of the pixel size of the concentration map, here 1 nm).

There are several ways to rationalize these observations: pores could form by agglomerations of oxygen vacancies resulting in a local excess of Zr and their surface could be decorated by Sn. If they contained gaseous H_2 , this would however not be detectable in APT because the gas molecules would escape from the pore when exposed to the vacuum during successive removal of ions from the specimen. We can rule out that these volumes are Zr hydrides, since the measured H fraction was below 1 at %. The larger feature in the centre (blue arrow) could also represent metal that is not fully oxidized, although it is not intuitively clear how this would come about.

3.2.3. Oxide-metal interfaces

Fig. 6 displays two datasets that captured the oxide-metal interface from (a) *Zircaloy-2* and (b) *Zircaloy-2 Fe+*, measured in LEAPs 3000X HR and 6000 XR, respectively. Fig. 6 (a₁) is an atom map of several O-containing ionic species. O_2^+ (32 Da) is a marker for ZrO_2 [29,30], $ZrO_2^{+}/+++$ ions are found inside suboxide (and at interfaces) and $ZrO^{+}/+++$ ions are the main O-containing species in APT of Zr metal (both in laser and voltage pulsing) with O in solid solution up to saturation. (a₂) is an atom map of Fe, Cr and Sn (no Ni at 29 Da was detected). Cr is very clearly, and Fe to some extent, clustered in the O-rich/O-saturated volume. The O concentration map in Fig. 6 (a₃) further highlights four regions of apparently different composition: ZrO_2 , ZrO , $Zr(O)_{sat}$, $Zr(O)$. The latter covers the compositional range between O-saturated metal (~29 at% O) and the bulk concentration of < 1 at%. Note that yellow represents 50 at% O (located between the 55 and 44 at% ICSs), and it is not of homogeneous thickness. Variations in the thickness and composition within the O-rich volumes are further highlighted in the O map depicted in Fig. 6 (a₅), which is viewed along the length axis of the reconstruction (section 'A-A'). The region outlined by a dashed red line labelled 'B' marks a somewhat peculiar case where O is locally lower than in the saturated metal although it is closer to the oxide. The proxigram in Fig. 6 (a₄) derived from a 50 at% O ICS in the volume highlighted by a grey box in (a₃) shows that O (blue line) in the oxide is slightly underestimated (consistent with APT data in [29,68,95]). Sn (green line) is slightly enriched at the interface between $Zr(O)_{sat}$ and ZrO_2 . The plateau in the O profile at ~30 at% marks the saturated Zr and from (a₅) it is clear that the width of this region is not of homogeneous thickness (here ~20–40 nm). The grey shaded area marks a region with a composition close to ZrO , the above-described artificial layer. Looking at the O maps in Fig. 6 (a₃) and (a₅) it is apparent that the 22 and 10 at% O ICSs are more serrated than the 44, 55 and 50 at% ICSs, i.e., the O ingress front into the bulk is not smooth on the nm level, or at

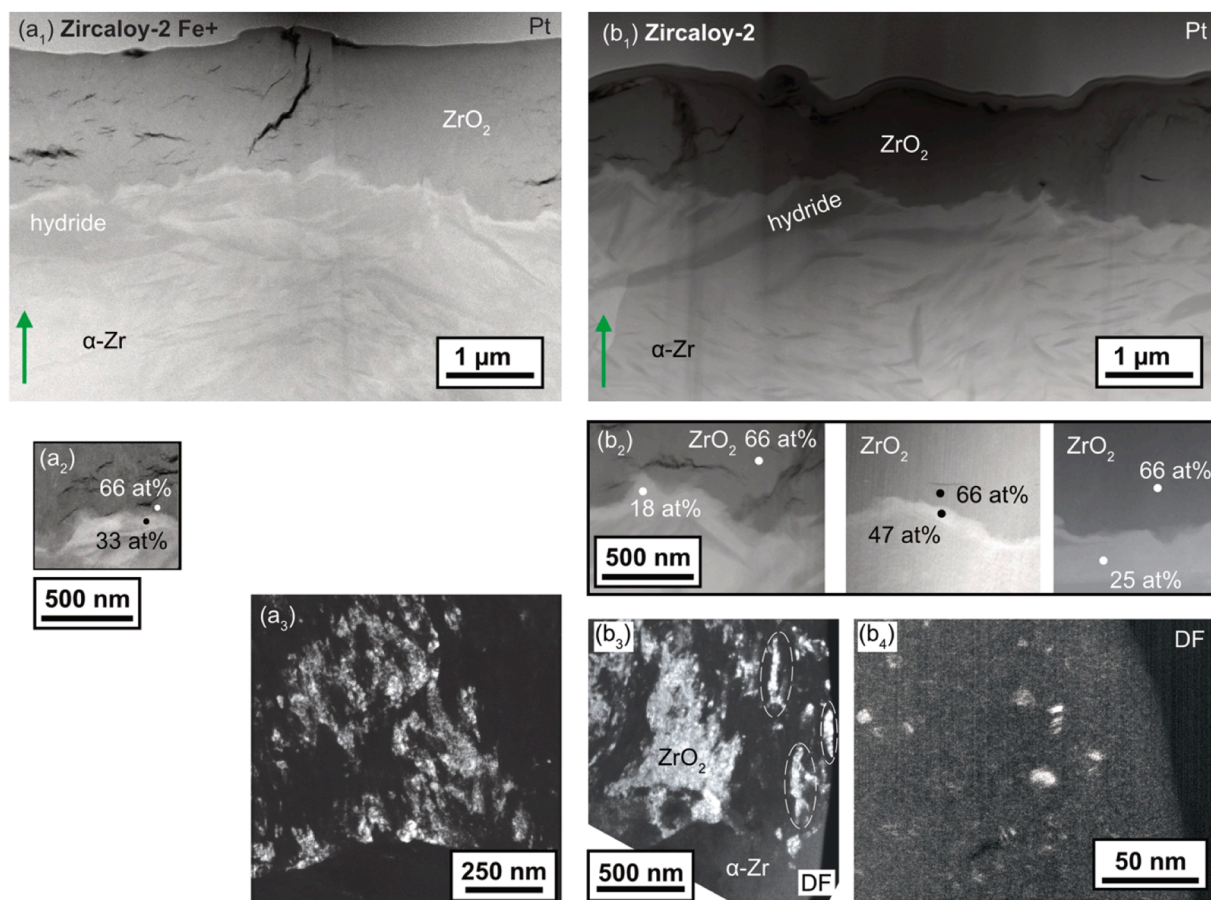


Fig. 3. TEM of oxide-metal interfaces, green arrows indicate the radial direction. HAADF images in (a) and (b) show many hydrides in the Zr metal, where the small ones are likely FIB-induced. At the interface a region with increased density is found, which is likely O-saturated α -Zr. This is confirmed by the EDS point measurements (a_2 , b_2) yielding approximately 20–50 at% O in the Zr. Centred dark-field (CDF) images show some columnar grains (a_3 , b_3) as well as some small more equiaxed grains (b_4).

the least less smooth in comparison to the oxide-metal interface.

Fig. 6(b) depicts a reconstruction of a second oxide-metal interface dataset, the largest we were able to collect. (b_1) is an atom map of Fe, Ni and O₂ with a 55 at% O ICS marking the interface between ZrO₂ and the metal. Fig. 6 (b_2) is the same view where O₂⁺ ions are omitted and Cr ions added. It is readily observable that fewer Fe and Ni ions are present in the oxide, which is *partially* due to the fact the 67 at% O are ‘diluting’ the initial metal composition. The Fe- and Ni-rich feature marked by an arrow (which is actually planar but depicted edge-on) marks what appears to be segregation to an oxide GB, but is more dilute than seen in GBs in non-irradiated material ([58,96] see also Fig. S3). The O map from a 10 nm thick slice in (b_3) illustrates that the oxide-metal interface again is relatively smooth while the 15 at% O ICS is serrated. The magnified rectangular view of the proxigram around the 50 at% O/Zr shows some deviation from an often-observed smooth transition at phase boundaries (see, e.g., [97]), see greyed area under the idealized curve towards the high-O side; this again is caused by the artificial ZrO layer. Like in the reconstruction presented in Fig. 6(a), Sn (green line) is rejected at the interface. The Sn fraction inside the oxide is, however, slightly larger in the oxide than in the metal (Table 4), and in addition Sn is clustered in the oxide as is highlighted by ICSs in Fig. 6 (b_5); the visibly higher number of Sn atoms at the boundary (black arrow) is partially owed to a density artefact (see density map in Fig. S4).

Table 4 is a comparison of the bulk concentrations of Fe, Cr, Ni and Sn of the unirradiated material and the composition determined from the oxide and metal volumes from Fig. 6(b). O was entirely excluded to compare the (normalized) fractions of the metallic alloying elements present in the two adjacent volumes. In the unirradiated condition the

matrix concentrations of Fe, Cr and Ni is only a few ten atomic ppm [56] as they are concentrated in SPPs. Their fraction after irradiation is hence a qualitative measure of the amount of SPP dissolution (with all the caveats given in [56]).

In the oxide, Fe and Ni fractions are significantly lower than in the adjacent metal. This means that Fe and Ni are actually ‘missing’ from the oxide. It is noteworthy that for Cr no such loss took place here. The Sn fraction was measured to be slightly higher in the oxide.

The apparent loss of Fe and Ni in the oxide directly adjacent to the metal (which was also reported in [47]), might be caused due to these elements being ‘pushed’ into the base metal.

Fig. 7 is an example of a case where Sn is almost entirely rejected from the oxide and clearly enriched at the interface (from the dataset shown in Fig. S1).

3.2.4. Metal adjacent to the oxide-metal interface

Fig. 8 shows a reconstruction capturing a region directly below the metal-oxide interface. This reconstruction only shows the part of the measurement in which an LPE of 50 pJ was used after passing the oxide-metal interface using 100 pJ; this section is depicted in Fig. S5 (a). The view in (a) is approximately parallel to the oxide-metal interface (see dashed line) and shows that close to the interface clustering of Fe and Cr is not as apparent as in the bulk. The O distribution is highlighted by 4, 7 and 20 at% ICSs in (a) and the corresponding ZrO ion map in (b). The depiction of the same reconstruction in (c), which is rotated about the length axis, shows the typical alignment of FeCr clusters (Fe+Cr ICS 4 at%) that is associated with rows of a-loops [98] (also referred to as *rafts* [99]; we have previously called them *layers* [53,57] because of their

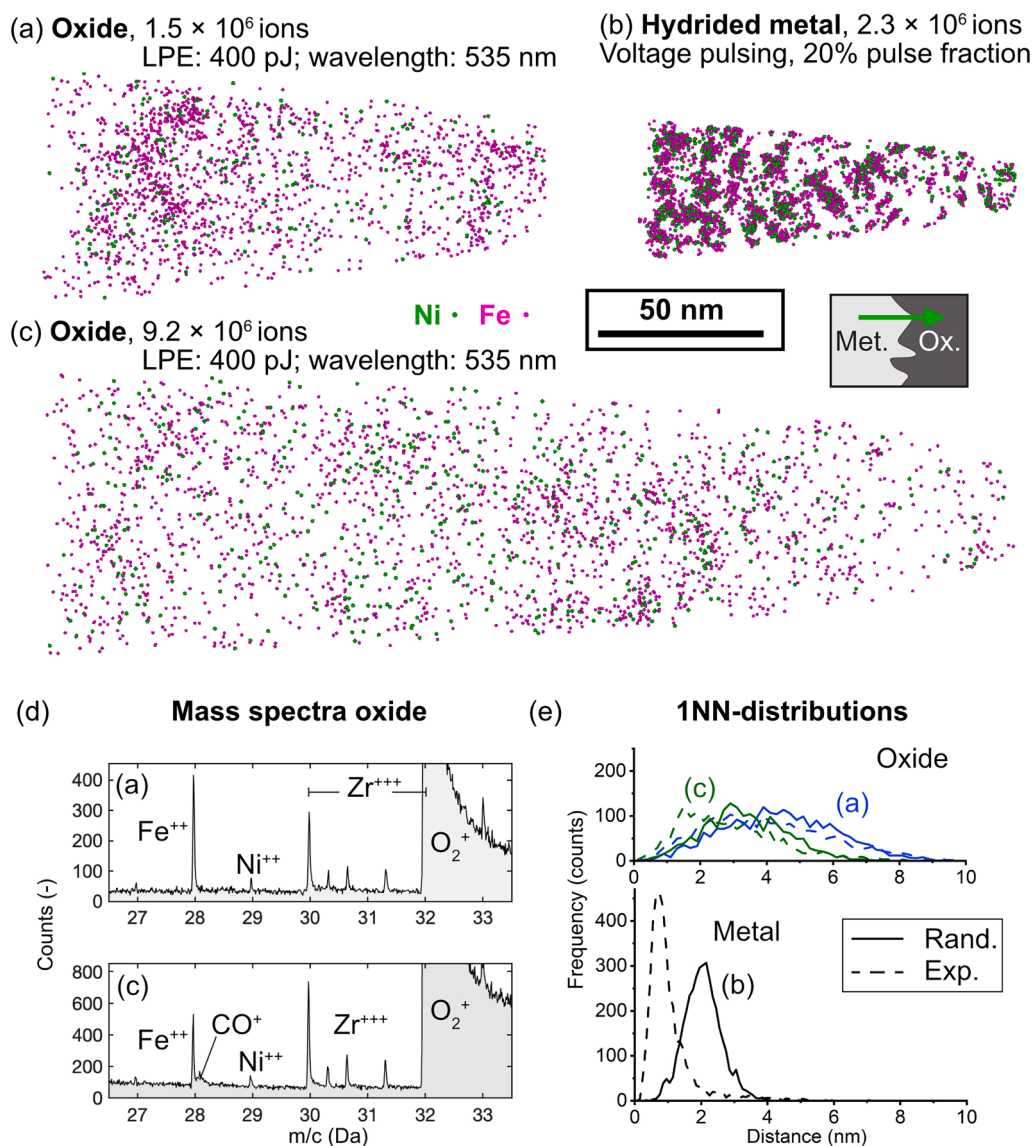


Fig. 4. Fe and Ni distribution in reconstructions from Zircaloy-2 Fe+: (a) and (c) are oxide and (b) is hydrided metal (FIB-induced). Sections from 26.6 to 33.5 Da of the mass spectra from the oxide measurements are shown in (d). (e) is a plot of the 1NN distributions of Fe+Ni for the three datasets. All measurements were performed in a LEAP 3000X HR with 70 K base temperature. Specimen axes are aligned with the radial direction of the tube.

extension in 3D visible in APT reconstructions). The composition profile across the oxide-metal interface in (a) is depicted in Fig. 8(d). The O-rich region (nearly saturated at ~ 28 at% at 0 nm) quickly drops to the approximate bulk composition of the material (Zircaloy-2). At the same time Fe and Cr increase (Fe above and Cr below the bulk value), an observation consistent with inward diffusion of these elements. The Sn fraction stays approximately at its bulk level. Fig. 8(e) is a plot of the composition in the c-direction showing Fe and Cr enrichment within the layers. The Fe and Cr maxima coincide with those of the O profile.

The dataset that is presented in Fig. 9 originates from a location inside the metal directly below the oxide-metal interface in a Zircaloy-2 Fe+ specimen. Fig. 9(a) shows Fe, Cr and O ICSs. Typical layered arrangement of Fe clusters parallel to the basal planes (see dashed lines) is found in the low-O region to the left of the ingressing O (see 3 at% O ICS). Cr clusters, which are fewer in number, are present in both the low-O region, where cluster layers are found, and in the high-O region towards the specimen apex. The 1D composition profile across the Fe cluster layers (Fig. 9(a)) depicted in (b) shows that Fe and O maxima coincide (similar to what is shown in Fig. 8(e)). In addition, the proxigram in Fig. 9(d) shows that within the layers, O is found to be increased

inside Fe clusters. These proxigrams were calculated for the largest Fe clusters identified by 1.7 at% ICSs. The O map in Fig. 9(c) highlights the O gradient from close to the oxide-metal interface into the bulk. In addition, there are two features in the high-O region that very clearly deviate from the remaining volume. Judging from the crystallographic orientation (shown in Figs. S6 and S7 and [78]) and Fe segregation behaviour (highlighted by ellipses in Fig. 9(a)) they resemble c-loops that are depicted edge-on. *c-loop 1* is surrounded by O-saturated Zr (~ 30 at%) while the volume inside it contains only around 5 at% O. *c-loop 2*, which is closer to the oxide-metal interface, exhibits nucleation of sub-oxide (ZrO) [78].

4. Discussion

The main objective of this work is to identify differences in material corroded inside a reactor in comparison with material from autoclave experiments, i.e., under the absence of radiation damage and connect these findings to potential mechanisms that can possibly explain the spectacular increase in oxidation rate and HPU with increasing flux [16, 100]. Since we did not observe differences between the Zircaloy-2 and

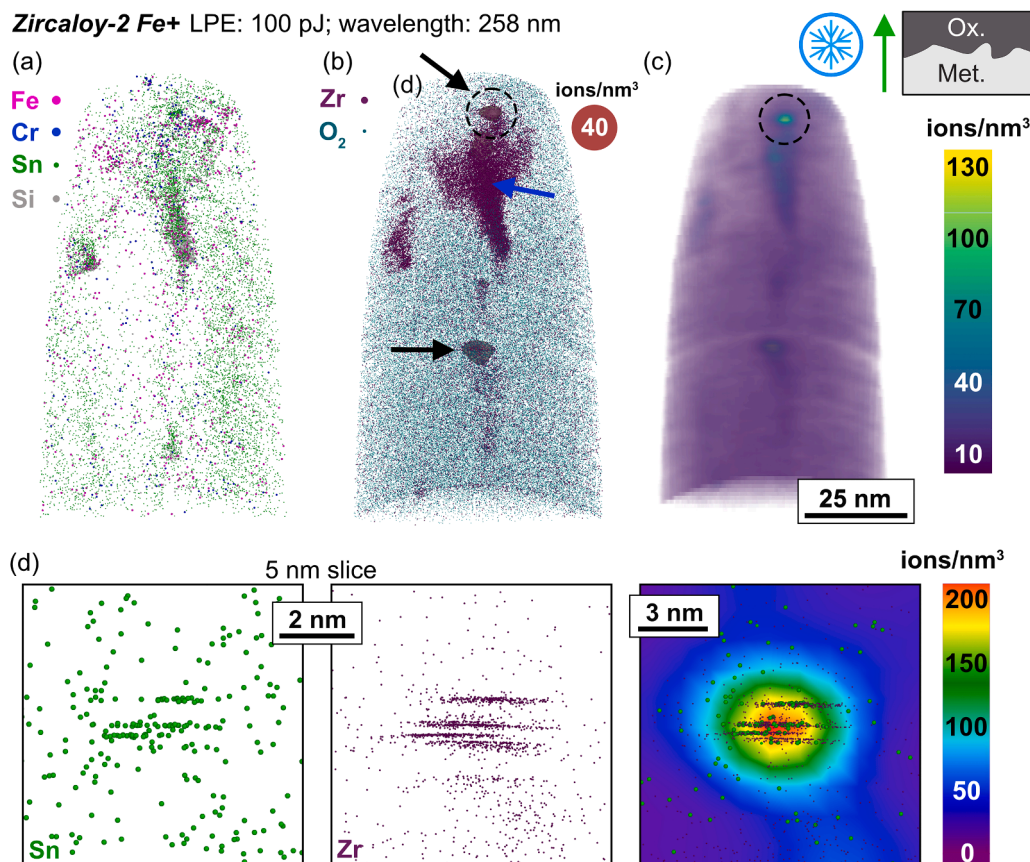


Fig. 5. Oxide with features of high ionic density presumably representing metal islands and pores that are rich in alloying elements and Zr. (a) and (b) are atom maps, (c) an ionic density rendering and (d) shows Sn and Zr ion distribution and an ionic density map around the alleged pore marked by a circle in (b) and (c), highlighting evidence of non-sequential evaporation and the ionic density. This specimen was prepared by cryo-FIB; specimen axis in radial direction.

Zircaloy-2 Fe+ tube, we do not distinguish between them in the discussion.

4.1. Oxide morphology

The crack morphology and distribution presented here are not qualitatively different from those reported in the literature from autoclave [101] and in-reactor corrosion [34]. Our observations of heterogeneous grain size and morphology are in agreement with those found in in-reactor-grown oxide scales by Garner et al. [34], who showed that in-reactor-grown ZrO_2 scales on Zircaloy-2 differ significantly from the well-defined columnar grains found in autoclaved materials. It is also reasonable to interpret the volumes of apparent high density in Fig. 5(c) as (partially connected) nanopores or nanotubes. This points to a potential effect that damage from neutron irradiation has on oxide growth and potentially enhanced diffusion of O and H because of an increase in interconnected porosity. While this train of thought is consistent, one should take note of autoclave experiments on Zr-Nb alloys that show increase of interconnected porosity and more complex grain morphology in post-transition compared to pre-transition scales [20], which is argued to be the reason for the higher corrosion rate in the post-transition regime (in autoclave). However, this is exactly what is proposed to be the difference between in-reactor- and autoclave-grown scales on Zircaloy-2 in [34] (in this context it is worth mentioning that the formation of (nano)porosity appears to be influenced by the presence of Li [46], which was present in the water in [20] but is not relevant for our samples as no Li is added to the water in Oskarshamn 3).

In any case, there is no clear difference between the oxide morphology from in-reactor and autoclave corrosion, which would explain the massive differences in performance.

4.2. Redistribution of alloying elements

While changes within the oxide scale in connection with cracking etc. and potentially radiation damage might play a role in the acceleration of corrosion, there exists convincing evidence that the damage to the base metal and the processes that it entails play a significant role [16, 102]. The most obvious difference in the microstructure is the radiation damage, which leads to redistribution of alloying elements from SPPs and also affects Sn. Hence, we now discuss the distribution of alloying elements after irradiation.

4.2.1. Elements originally located in SPPs: Fe, Ni, Cr

During irradiation Fe, Ni and Cr are redistributed from $Zr(Fe,Cr)_2$ and $Zr_2(Fe,Ni)$ SPPs [51,54,55,59,74,77,79] at different velocities due to the difference in diffusivity [103]. The very low solubility of < 10 ppm of these elements in α -Zr [56] leads to segregation at defects such as dislocation loops and (sub-)GBs. In the base metal (away from the oxide-metal interface) the local concentration of Cr (clusters) is mainly depending on the proximity to $Zr(Fe,Cr)_2$ SPPs [53,59], owing to the slower diffusion of Cr [103]. In contrast, FeNi clusters were present almost throughout the entire volume in more than 100 APT measurements we performed on irradiated fuel cladding in our previous studies [53,56–58,77,79] and in APT measurements presented in the further literature [51,54,55,59,74] (one example is displayed in Fig. 4(b), see also Fig. S8). The experimental evidence illustrated in Figs. 4, 6(b), 8 and 9(a) shows that the distribution of Fe and Ni has distinct appearances in the oxide, the O-rich region and the metal. As mentioned above, FeNi as well as FeCr clusters at a-loops are clearly visible throughout the metal. In the O-enriched volumes (i.e., above ~ 2–3 at% O vs. bulk concentration of ~ 0.7 at% O in the as-produced metal) like in Figs. 6(b),

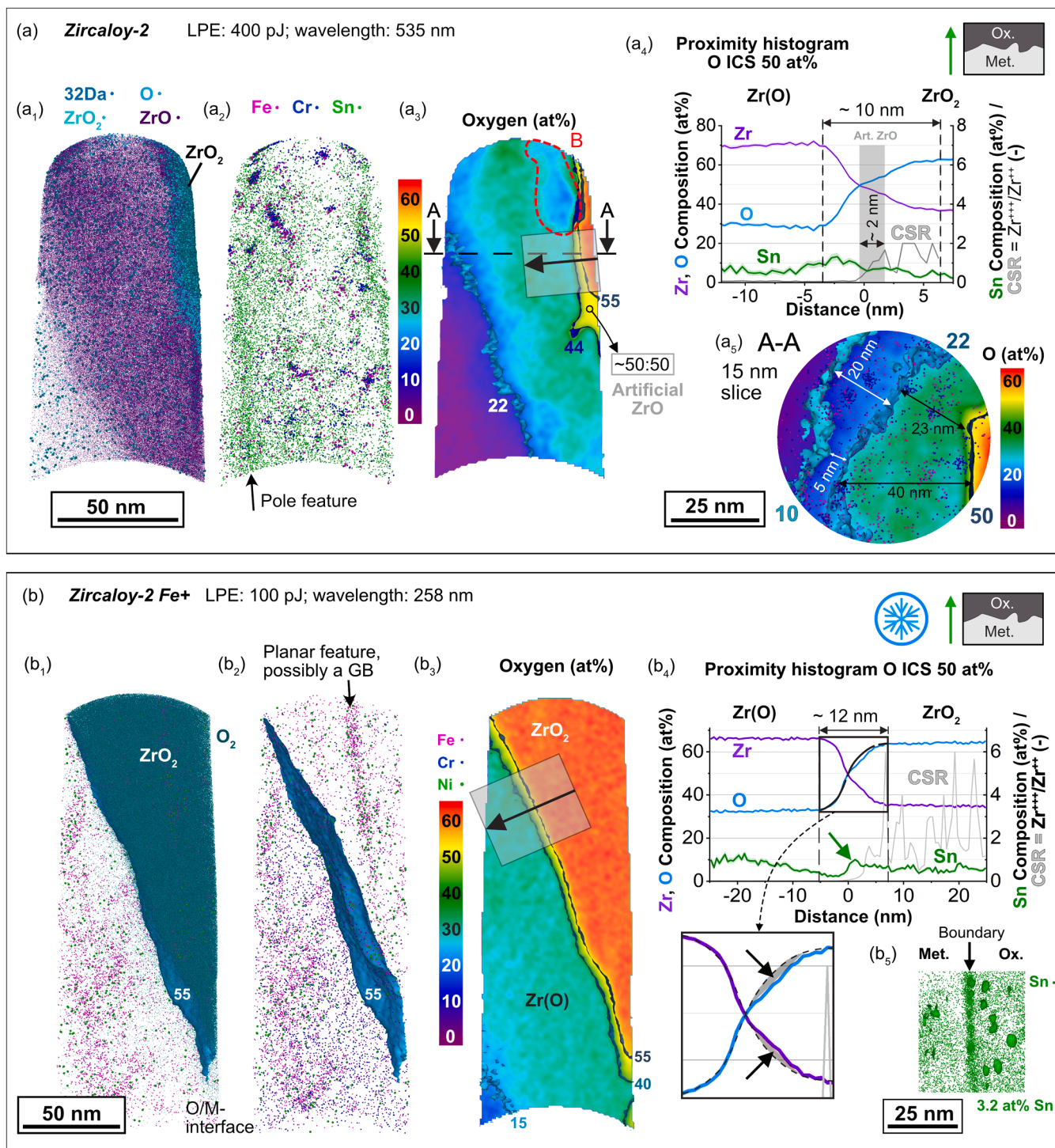


Fig. 6. APT measurement capturing the oxide-metal interface with a significant ZrO_2 volume. (a) A reconstruction that captures nearly the entire interface from the ZrO_2 to the base metal (see proxigram in (a₄)). (b) A reconstruction that captures a large volume around the interface between oxide and O-rich metal where Sn seems to be rejected. Numbers in the images are ICS values.

8 and 9(a), there is still some non-random distribution of Fe and Ni but clearly isolated clusters are not (or no longer) present. The non-randomness is even less pronounced in the oxide, as seen in Figs. 4 and 6(b). Although there appears to be enrichment at a planar feature (presumably an oxide grain boundary) in Fig. 6(b), and possibly some enrichment at what could be boundaries in Fig. 4, there is no evidence of clustering similar to what is seen in the metal. It thus appears that when interstitially diffusing O atoms ingress into the metal they compete with interstitially dissolved Fe, Ni and Cr for the same atomic positions

(mostly octahedral sites, although Cr can also be substitutional [104, 105]) close to or at defects. O has a higher affinity to Zr than the transition metals, and one can argue that it should displace them in the site competition. Since the solubility of the transition metals is low inside ZrO_2 it is reasonable to assume that they move into the metal matrix (further) enriching irradiation-induced defects there. It appears that some Cr-rich clusters remain, as seen in Figs. 6 (a₂) and 9(a) (see 1.1 at% ICSs in the O-saturated regions), and this can be explained by its lower diffusivity and potentially by the fact that O is not displacing it if it

Table 4

Comparison of the bulk concentration of Zircaloy-2 Fe+ and the compositions obtained by APT (in at%) from the dataset in Fig. 6(b); O has been entirely excluded from the composition analysis.

	Fe	Cr	Ni	Sn	Zr ³⁺ / Zr ²⁺
Bulk concentration as-produced Zry-2 Fe+	0.58	0.31	0.10	1.00	-
Composition from the oxide region by APT (54 at% ICS, O excl.)	0.26	0.23	0.03	1.21	1.712
Composition from the metal region by APT (55 at% Zr ICS, O excl.)	0.54	0.23	0.09	1.00	0.001

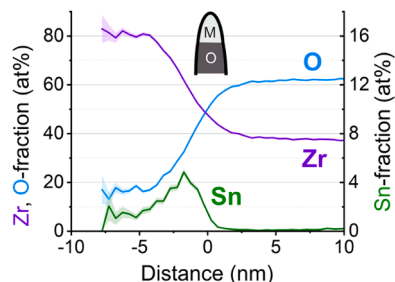


Fig. 7. Example of a proxigram showing rejection of Sn (from the dataset shown in Fig. 1 (b)).

occupies substitutional sites. A flux of transition metals into the bulk metal from Zr(O) could explain the relatively lower fraction of Fe and Ni in ZrO₂ (Table 4, see also [66]). The remaining transition metal atoms are then incorporated into ZrO₂ when the oxidation front arrives, leaving only volumes of slightly increased Fe and Ni content in the matrix.

Since the grain size is very small it is unlikely that we did not capture any GBs, which means that GB segregation in irradiated oxide might be reduced compared to autoclave exposure [31]. We found one rather diffuse planar arrangement of Fe and Ni that might resemble GB segregation of Fe and Ni (see Fig. 6(b)). This feature could be the remnant of a metal GB containing Fe and Ni segregation that was incorporated into the oxide, as has been previously observed in autoclave-tested material [96]. However, the results might be explained by an alternative and – in our view – more likely explanation, namely that this represents segregation by diffusion of Fe and Ni to a GB inside ZrO₂, since it is unlikely that clusters of Fe, Ni and Cr dissolve but the same elements located at GBs would stay in place. In this scenario, the GB (visible in Fig. 5(b)) would have been created during the last few days of reactor service (around 2 to 10 days assuming a constant oxide growth rate). This should be possible since Fe and Ni are not interstitially dissolved in the oxide but substitutionally (cations) and are therefore affected by the radiation-induced vacancy concentration that increases diffusion substantially. A diffusion length from matrix to GB of say 10 nm in two days requires a diffusion constant of around 10⁻²² m²s⁻¹, which is a reasonable value at our damage rate (2·10⁻⁷ dpa s⁻¹) and sink density (2·10¹⁵ m⁻² for a grain size of 20 nm). What is in favour of this construal is that segregation is relatively clear away from the interface into ZrO₂ and nearly vanishes when coming closer to the interface, which is the oxide that is expected to have formed last and hence segregation could not have taken place yet.

4.2.2. Sn in ZrO₂

Sn clustering – which also takes place in autoclave corrosion, albeit at slightly increased temperatures (360 °C) [65] – is shown in Fig. 6 (b₅) in proximity to the interface. It is most pronounced at the interface and also present in the ZrO₂ in direct vicinity to the interface; a few very

small clusters can also be seen in the Zr(O)_{sat}. A potential interpretation is that initial clustering (or precipitation) takes place during O ingress into the metal. These Sn-rich volumes remain in a metallic state as they are not being oxidized (immediately) due to the very low O potential at the metal-oxide interface [106]. Furthermore, the proxigram in Fig. 7 exhibits a clear Sn increase at the purported interface location, indicating partitioning at the oxide-metal interface. The example in Fig. 6 (b₄) is less clear, but here too, an increase in Sn fraction right at the phase boundary is found. Rejection at the interface/partitioning into the metal requires comparatively high mobility which is likely irradiation-assisted since substitutional elements like Sn otherwise would not be mobile at reactor operating temperature [103]. Comparisons of the Sn behaviour in reactor and in autoclave might be of limited value because the mobility in the latter case is brought about by increased temperature.

None of our observations provides an obvious explanation of the faster corrosion of Zr-Sn alloys compared to those without (or with lower) Sn fractions [107]. At the same time, the role that Sn does play in the stabilization of tetragonal as opposed to monoclinic ZrO₂, especially at the oxide-metal interface does not appear to be clear. In Nb-containing alloys lower Sn contents are associated with lower tetragonal ZrO₂ fractions [108], while in Zircaloy-4 type alloys (more similar to the here investigated Zircaloy-2 type alloys) lower Sn content is associated with higher tetragonal ZrO₂ fractions [107]. In order to shed light on this, local concentrations inside the oxide (or variations therein) as well as its structure would need to be assessed, which based on the here reported results is challenging if not infeasible.

4.3. Relevance of experimental observations for the in-reactor oxidation

4.3.1. Oxygen ingress

The formation of ZrO₂ relies on the transport of O through the oxide scale – that includes the non-protective oxide and the active barrier layer – and the diffusion into the metal. These are discussed in light of the experimental observations.

4.3.1.1. O transport through the oxide. The experimental observations (different oxide morphology and porosity) here (see Fig. 3) and elsewhere may explain some increase of the in-reactor corrosion rate, but they are not qualitatively different and do not obviously explain a flux-driven acceleration: The supply of O across the outer oxide in the posttransition regime is likely taking place via water ingress through cracks and interconnected porosity. Since the grain size is in the order of a few to some hundred nm, the transport of O (or OH⁻) through the barrier layer via GB diffusion [20,109] is accelerated. The increase in transport capacity via GBs, which also takes place in autoclave, does, however, not explain the massively increasing corrosion rates in reactor.

One other factor that affects oxygen ingress is the lateral cracks formed in the oxides, since these provide a faster diffusion path for oxygen than GB diffusion [101]. In autoclave testing of Zircaloy-2 the total lateral crack area was found to depend on the mean size of the SPPs, leading to a higher crack area and faster oxidation for smaller SPPs [101]. Since SPPs gradually dissolve during irradiation, this effect could contribute to gradually faster O transport through the oxide during reactor service. However, it is difficult to believe that this effect could result in a rather sudden acceleration of in-reactor corrosion.

4.3.1.2. O diffusion into the metal. Suboxide has not been found in any of our APT measurements of the oxide-metal interface (Figs. 3, 6, S5). This is expected to be the case in the post-transition regime and is not a specific observation for in-reactor corrosion. Its absence is likely necessary for accelerated corrosion in both autoclave and reactor to occur. In the metal, O diffuses interstitially and should only be slightly affected by the presence of vacancies created through damage cascades, i.e., bulk diffusion is likely not significantly enhanced. The following

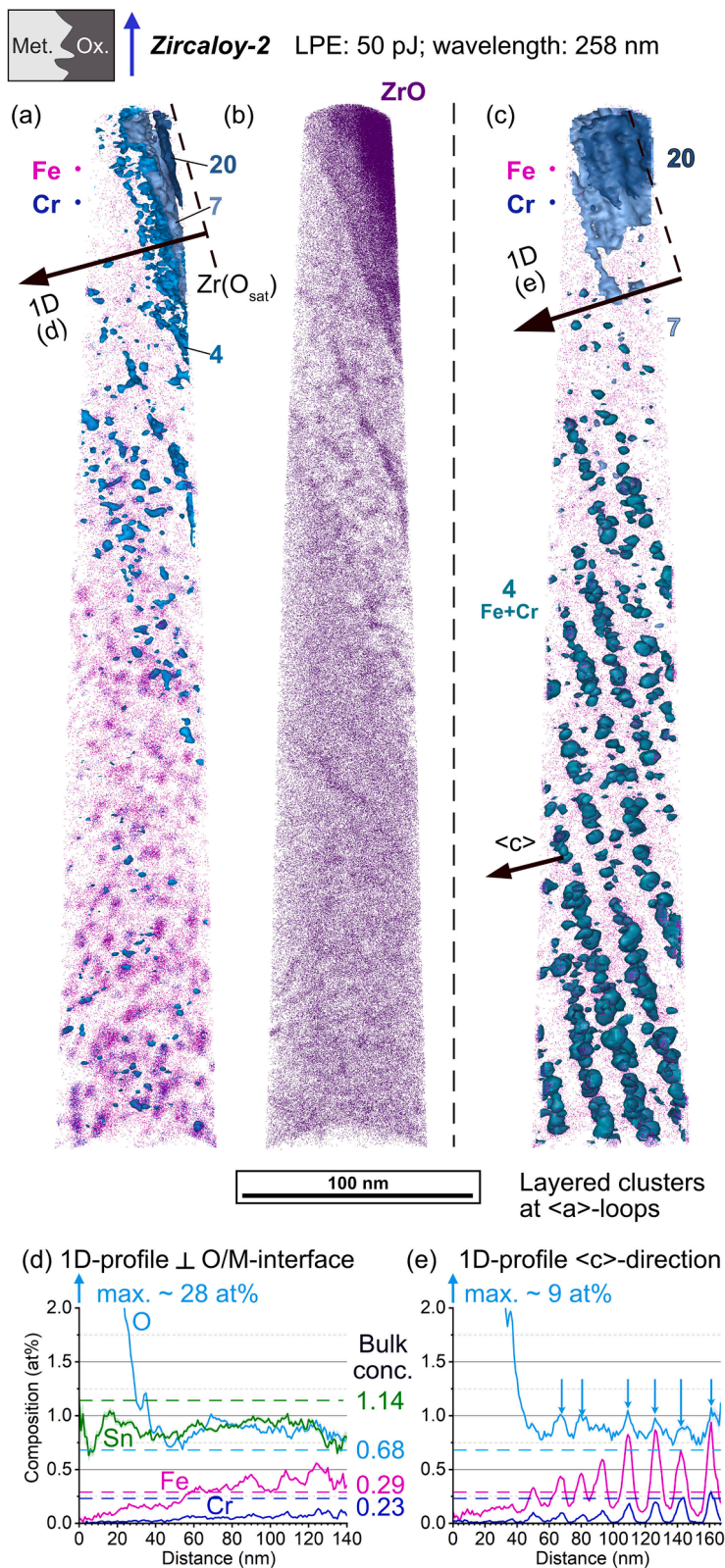


Fig. 8. Solute distribution in proximity to the oxide-metal interface in Zircaloy-2. Less FeCr clusters are present near the O-rich region. (a) oxide-metal interface edge-on, (b) ZrO ion map with the same orientation, (c) view with clusters aligned parallel to basal planes. Digits in (a) and (c) indicate the values for color-coded O-ICSSs, a 4 at% Fe+Cr ICS highlights FeCr clusters in (c). (d) 1D composition profile perpendicular to the oxide-metal interface and (e) along the <c>-direction, see arrows and dashed lines in (a) and (c).

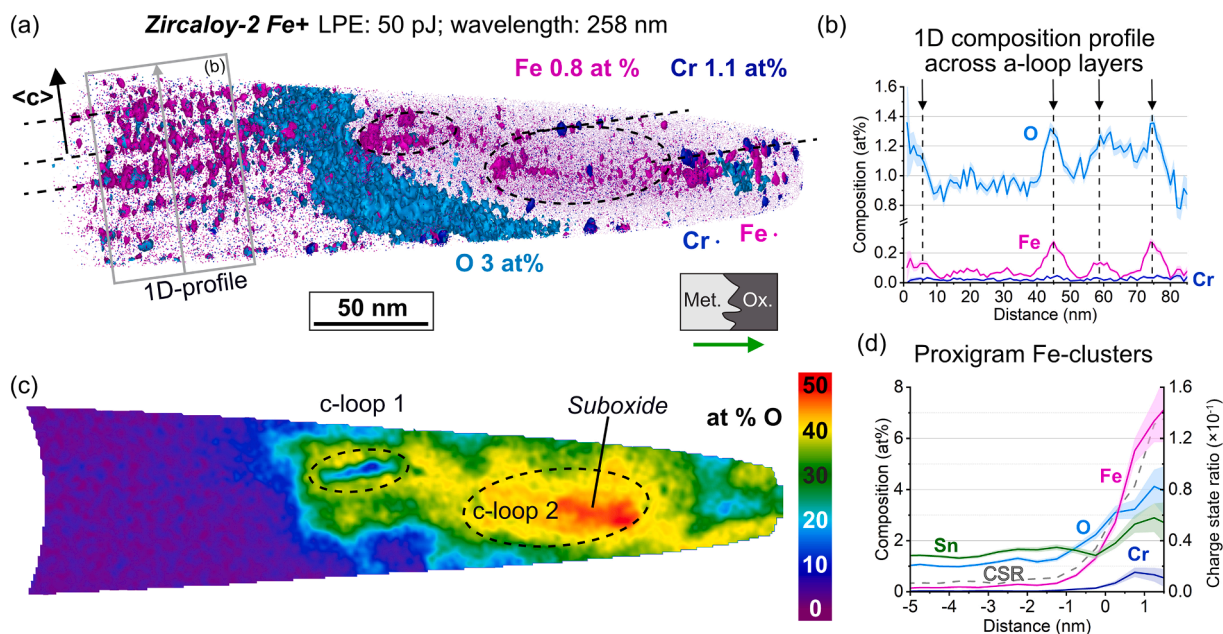


Fig. 9. Formation of suboxide at c-loops in the metal close to the metal-oxide interface. (a) Fe clusters are only present in the low-O region, while Cr clusters remain in the high-O region. (b) 1D profile across cluster layers shows that O is enriched in layers coinciding with layers of Fe clusters. (c) O composition map, showing the ingress into the metal. (d) proxigram of Fe clusters.

findings regarding the O diffusion into the metal are worth mentioning:

Firstly, the O-saturated region, $Zr(O)_{sat}$, between the oxide and the base metal, has a variable width (10–50 nm according to our APT data), after which the O fraction declines until reaching the bulk concentration of below 1 at%. This width is smaller than in pre-transition [68] and similar to post-transition autoclave corrosion in other Zr alloys [21,29,30]. In the transition region from $Zr(O)_{sat}$ to $Zr(O)$ we find a serrated growth front (Fig. 6 (a₃) and (a₅)) similar to what has been shown in, e. g., [7,29]. Our results hence tie nicely into what is known from cited studies above and does not indicate a difference between autoclave and in-reactor corrosion in this regard.

Secondly, the width of the O diffusion profile from saturated Zr to the bulk concentration seems to be consistent with bulk diffusion similar to autoclave testing at 400 °C [110]. Since O is supposed to diffuse interstitially in Zr, a direct effect of vacancy generation by radiation is not expected (as opposed to the large increase of mobility for substitutionally diffusing elements like Sn). There is only a small amount of published APT and EELS data capturing the diffusion profile below the saturated $Zr(O)_{sat}$, but these studies [21,29,110] do not show large differences to what we have found, namely the decrease from ~ 29 at% to the bulk concentration of O takes place within maximum 100 nm. The non-planar nature of these ‘interfaces’ (see also Fig. S9) makes quantification challenging (and impossible in STEM-EELS and -EDS), but the observed depths of the O profile does not indicate increased bulk diffusion.

4.3.1.3. O interaction with dislocation loops in the damaged metal.

Finally, our investigations reveal interactions of O and dislocation loops (identified in APT based on segregation patterns and crystallography [77,78,111]): layers of a-loops near the oxide-metal interface have increased O fractions (see Figs. 8 and 9), indicating that O is preferentially located in the vicinity of dislocation loops (possibly in the strain field) and might be the reason why transition metal clusters dissolve. This means that O diffusion could be enhanced within the cluster layers, i.e., increased diffusion within the basal plane, while normally diffusion in the c-direction (i.e., the perpendicular direction) is faster [103,112]. However, a-loops appear early and their number saturates [113] long before accelerated corrosion takes place, and hence it is unlikely that

they play a significant role in the acceleration of corrosion at high fluence. In addition, we have shown that they disappear in the O-saturated volume ahead of the oxide-metal interface.

Two other aspects of damage, however, do become more pronounced at higher damage levels: (i) SPP dissolution proceeds and hence precipitates become smaller while the amount of Fe, Cr and Ni in the Zr matrix increases [56,59] and (ii) the formation of c-loops, which emerge at about 5 dpa [44,114] and evolve over much longer periods of irradiation [115].

The release of Fe from $Zr(Fe,Cr)_2$ -SPPs appears to be largely complete already at low fluence (4 dpa [54]) and hence Fe release is likely not decisive for the acceleration of corrosion. Even the later release of Fe and Ni from the $Zr_2(Fe,Ni)$ -SPPs is probably not so important either, since much less Fe is bound to this phase that additionally does not fully dissolve even after long time. However, we want to make our case based on the observation of suboxide nucleation inside a c-loop: in a singular case we identified a c-loop as the location of (sub)oxide inside the metal (‘c-loop 2’ in Fig. 9) and can state that direct interaction of O with defects does take place. Upon eventually transforming into ZrO_2 this will lead to a significant localized volume increase, which can initiate localized damage to the barrier oxide so it loses its protective capability. If this happens at multiple locations it could lead to significant cracking and accelerated oxidation (which presumably is further enhanced by interaction with more loops). We also want to make note of the fact that the volume of O-saturated Zr is larger (or reaches ‘deeper’, approximately 200 nm) than in the other instances where we captured oxide-metal interfaces or where they are shown in the literature [21,29,110]. Last, it is noteworthy that the c-axis of the specimen in Fig. 9 is nearly perpendicular to the radial direction, which is a rare orientation for Zircaloy cladding tubes [116] and could be relevant since corrosion behaviour is texture dependent as described by Garner et al. [117].

While this is an interesting scenario, it has to be rationalized in light of the observation of a further c-loop (‘c-loop 1’ in Fig. 9) located in close vicinity appears to be ‘protected’ from oxidation by an Sn shell that formed after it was rejected from the volume inside the loop. One possibility is that the pure Zr volumes such as found inside c-loop 1 could constitute nucleation sites not only for oxides but also for hydrides.

4.3.2. Acceleration of hydrogen pickup

The positive effect of higher Fe concentration is demonstrated by the fact that the *Zircaloy-2 Fe+* tube showed lower HPU than the *Zircaloy-2* tube [118]. This observation is in line with the described positive effect that Fe has over Ni on HPU [119], when present at GBs. If one assumes that the oxide of the *Zircaloy-2 Fe+* tube contains more Fe (and hence has a higher Fe/Ni ratio) than that of the *Zircaloy-2* and – like for O ingress – H ingress is taking place by GB diffusion [20,95], Fe and Ni at the oxide GBs could still explain the difference between the alloys although less pronounced segregation under irradiation compared to autoclave corrosion counteracts the positive effect that Fe has on HPU.

In addition to acceleration of H ingress by GB diffusion, voids or metal islands in the oxide close to the interface can potentially act as pathways for H ingress and short-circuit the active oxide similar to nano-voids and -pipes proposed by Lindgren and Panas [120] and others [48]. Again, these factors can probably not account for the massively increased in-reactor behaviour, since porosity and inhomogeneous grain morphologies (with likely larger GB areas) are also found in autoclave corrosion. The presence of pores or metal islands with sizes of a few nm has been shown close to oxide-metal interfaces by TEM [20,121]. Our results can be construed as confirmation of their presence, adding the new insight that they have a distinct chemistry differing from that of the oxide. The alleged presence of such pores is not in conflict with the proposed HPU mechanism put forth in [120], but the features we observed are likely much larger than the ones proposed there namely, accumulation of a few neutral oxygen vacancies. Since diffusion of Sn is limited in the oxide it seems reasonable to assume that potentially incomplete Sn coverage on the inside of such larger pores leaves the possibility of termination by H and a HPU process similar to that proposed in [120], although we do not have experimental evidence for this.

Again, differences in the oxide nano-chemistry do not explain the reason that HPU (alongside oxidation) is accelerated by the level of damage to the metal. We hence propose that the reasoning regarding the increase of oxidation rate in the previous section is essentially also valid for HPU: the breakdown of the protective capacity of the scale through internal oxidation allows for fast H uptake. While there is some evidence that $Zr_2(Fe,Ni)$ precipitates or the Zr matrix around $Zr(Fe,Cr)_2$ precipitates can act as hydrogen traps in non-irradiated Zr alloys [122,123], hydride formation or increase in H fraction in $Zr(Fe,Cr)_2$ precipitates was not found in irradiated metal by APT [78]. Furthermore, because SPPs dissolve and their number decreases with burnup it seems counterintuitive to assume that they contribute to a massive increase in HPU as they disappear. Therefore, we want to propose that analogous to the nucleation of suboxide inside c-loops (Fig. 9) hydride nucleation at c-loops can take place. Since H diffuses deeper into the metal than O, this might lead to a scenario in which large numbers of hydrides precipitate below the layer in which (sub)oxide nucleation takes place. Because of the texture (c-axis mostly aligned in radial direction) hydrides are mostly tangentially aligned and due to the volume increase add to the stresses on the interface exerted by the (sub)oxides further degrading the integrity of the barrier layer.

5. Conclusions

Zr-based fuel claddings show significant acceleration of corrosion in reactor compared to autoclave (or zero flux) conditions. Since this behaviour is also connected to the damage accumulation inside the metal and not just to the protective oxide, a mechanistic understanding of the oxidation at the oxide-metal interface is needed. APT is currently the only characterization technique capable of analysis with sufficient spatial resolution in 3D while providing elemental identification within the probed volume.

- We therefore conducted more than 50 APT experiments targeting the oxide-metal interface.

- Oxide and oxide-metal specimens are not often successfully measured in APT (we had around 20 % useful measurements).

These are the key findings and conclusions from the present work:

- Clusters of Fe, Ni and – after longer time – Cr start to dissolve in O-rich metal. When incorporated into the oxide these clusters are almost fully dissolved, giving a rather even distribution of Fe and Ni inside the oxide. In addition, the concentrations of Fe and Ni are reduced inside the oxide, which is likely caused by a migration into the metal ahead of the oxidation front.
- GB segregation of Fe and Ni (but not Cr) takes place in the oxide by irradiation-induced diffusion, but is much less pronounced than in autoclave corrosion. This means that the positive effect of Fe GB segregation on HPU is possibly reduced under irradiation.
- Pores or metal islands inside the oxide are associated with local O deficiency (higher Zr, Sn and transition metal concentration in their vicinity). This opens the possibility of pores playing a role in a process of HPU by short-circuiting the scale, similar to what is presented in [120].
- Sn seems not to play a significant role in the oxidation process directly, since it, likely due to its irradiation-assisted mobility, is rejected both on a larger (partitioning into the metal at the oxide-metal interface) and a smaller scale (clustering in ZrO_2).
- No ZrO suboxide was found at the oxide-metal interface by APT.
- The very strong acceleration of in-reactor corrosion at high damage levels is potentially caused by the interaction of O with c-loops, where we observed suboxide formation ahead of the oxidation front.
- HPU might be influenced by similar factors as oxidation, especially the interaction with damage inside the metal, namely, dislocation loops. Additionally, pores within the oxide could play a role in ‘short-circuiting’ the barrier oxide leading to increase in HPU as proposed in the literature.

CRediT authorship contribution statement

David Mayweg: Writing – review & editing, Writing – original draft, Visualization, Investigation, Formal analysis, Data curation, Conceptualization. **Johan Eriksson:** Writing – review & editing, Investigation, Data curation. **Mohammad Sattari:** Writing – review & editing, Investigation, Data curation. **Hans-Olof André:** Writing – review & editing, Supervision, Formal analysis. **Mattias Thuvander:** Writing – review & editing, Supervision, Resources, Project administration, Investigation, Funding acquisition.

Declaration of competing interest

The authors declare that they have no known competing financial interests or personal relationships that could have appeared to influence the work reported in this paper.

Acknowledgments

DM acknowledges funding from the Swedish Centre for Nuclear Technology (SKC). WSE, VF, OKG, EPRI are acknowledged for financial contributions. We are thankful to Itai Panas for engaging discussions regarding oxidation, corrosion and hydrogen pickup of zirconium. We thank Magnus Limbäck and Pia Tejlund for provision of the cladding tube samples, Olof Bäcké for support with TEM operation, the MIDAS and MUZIC 3 communities for collaboration. All experiments were performed at Chalmers Materials Analysis Laboratory (CMAL).

Supplementary materials

Supplementary material associated with this article can be found, in the online version, at [doi:10.1016/j.actamat.2025.121020](https://doi.org/10.1016/j.actamat.2025.121020).

References

- [1] C. Lemaignan, Corrosion of zirconium alloy components in light water reactors, in: S.D. Cramer, B.S. Covino Jr (Eds.), *Corrosion: Environments and Industries*, ASM International, 2006, pp. 415–420.
- [2] V.F. Urbanic, B.D. Warr, A. Manolescu, C.K. Chow, M.W. Shanahan, Oxidation and deuterium uptake of Zr-2.5Nb pressure tubes in CANDU-PHW reactors, in: L.F.P. Van Swam (Ed.), *Zirconium in the Nuclear Industry: Eighth International Symposium*, ASTM International, West Conshohocken, PA, 1989, pp. 20–34.
- [3] P. Chemelle, D.B. Knorr, J.B. Van Der Sande, R.M. Pelloux, Morphology and composition of second phase particles in zircaloy-2, *J. Nucl. Mater.* 113 (1) (1983) 58–64.
- [4] X. Meng, D.O. Northwood, Second phase particles in Zircaloy-2, *J. Nucl. Mater.* 168 (1) (1989) 125–136.
- [5] M. Inagaki, M. Kanno, H. Maki, Effect of alloying elements in zircaloy on photo-electrochemical characteristics of zirconium oxide films, in: A.M. Garde (Ed.), *Zirconium in the Nuclear Industry: Ninth International Symposium*, ASTM International, West Conshohocken, PA, 1991, pp. 437–460.
- [6] O. Kubaschewski, B.E. Hopkins, *Oxidation of Metals*, Butterworths Scientific Publishing, London, 1953.
- [7] P. Tejlund, H.-O. Andrén, Oxidation induced localized creep deformation in Zircaloy-2, *J. Nucl. Mater.* 444 (1) (2014) 30–34.
- [8] B. Cox, Some thoughts on the mechanisms of in-reactor corrosion of zirconium alloys, *J. Nucl. Mater.* 336 (2005) 331–368.
- [9] F. Garzarolli, Y. Broy, R.A. Busch, Comparison of the long-time corrosion behavior of certain Zr alloys in PWR, BWR, and laboratory tests, in: G.P. Sabol (Ed.), *Zirconium in the Nuclear Industry: Eleventh International Symposium*, 1996, pp. 850–864. ASTM International, West Conshohocken, PA.
- [10] J. Romero, L. Hallstadius, M. Owaki, G. Pan, K. Kataoka, K. Kakiuchi, R. J. Comstock, J. Partezana, A. Mueller, M. Dahlbäck, A. Garde, A. Atwood, M. Åslund, Evolution of westinghouse fuel cladding, *Proceedings of WRFPM/TopFuel*, Sendai, 2014.
- [11] W. Goll, L. Ray, The behavior of intermetallic precipitates in highly irradiated BWR LTP cladding, in: P. Rudling (Ed.), *Zirconium in the Nuclear Industry: Thirteenth International Symposium*, ASTM International, West Conshohocken, PA, 2002, pp. 80–95.
- [12] F. Garzarolli, R. Schumann, E. Steinberg, Corrosion optimized zircaloy for boiling water reactor (BWR) fuel elements, in: E.R. Bradley (Ed.), *Zirconium in the Nuclear Industry: Tenth International Symposium*, ASTM International, West Conshohocken, PA, 1994, pp. 709–723.
- [13] K. Kakiuchi, K. Ohira, N. Itagaki, Y. Otsuka, Y. Ishii, A. Miyazaki, Irradiated behavior at high burnup for HiFi alloy, *J. Nucl. Sci. Technol.* 43 (9) (2006) 1031–1036.
- [14] Y.E. Ishimoto, T. Matsumoto, D. Lutz, A. Takagi, Improved Zr alloys for high burn-up BWR fuel, *TopFuel*, Salamanca, 2006.
- [15] E. Hillner, Long-term in-reactor corrosion and hydriding of zircaloy-2 tubing, in: D.G. Franklin (Ed.), *Zirconium in the Nuclear Industry*, ASTM International, West Conshohocken, PA, 1982, pp. 450–478.
- [16] B.F. Kammenzind, J.A. Gruber, R. Bajaj, J.D. Smee, Neutron irradiation effects on the corrosion of zircaloy-4 in a pressurized water reactor environment, in: R. J. Comstock, A.T. Motta (Eds.), *Zirconium in the Nuclear Industry: 18th International Symposium*, ASTM International, West Conshohocken, PA, 2018, pp. 448–490.
- [17] J.H. Schemel, Parametric study of an autoclave test for nodular corrosion, in: L.F. P. Van Swam (Ed.), *Zirconium in the Nuclear Industry*, ASTM International, West Conshohocken, PA, 1987, pp. 243–256.
- [18] E. Hillner, Corrosion of zirconium-base alloys—an overview, in: G.W. Parry (Ed.), *Zirconium in the Nuclear Industry*, ASTM International, West Conshohocken, PA, 1977, pp. 211–235.
- [19] M.B. Elmoselhi, B.D. Warr, S. McIntyre, A study of the hydrogen uptake mechanism in zirconium alloys, in: E.R. Bradley (Ed.), *Zirconium in the Nuclear Industry: Tenth International Symposium*, ASTM International, West Conshohocken, PA, 1993, pp. 62–79.
- [20] J. Hu, T. Aarholt, B. Setiadinata, K. Li, A. Garner, S. Lozano-Perez, M. Moody, P. Frankel, M. Preuss, C. Grovenor, A multi-technique study of “barrier layer” nano-porosity in Zr oxides during corrosion and hydrogen pickup using (S)TEM, TKD, APT and NanoSIMS, *Corros. Sci.* 158 (2019) 108109.
- [21] N. Ni, D. Hudson, J. Wei, P. Wang, S. Lozano-Perez, G.D.W. Smith, J.M. Sykes, S. S. Yardley, K.L. Moore, S. Lyon, R. Cottis, M. Preuss, C.R.M. Grovenor, How the crystallography and nanoscale chemistry of the metal/oxide interface develops during the aqueous oxidation of zirconium cladding alloys, *Acta Mater.* 60 (20) (2012) 7132–7149.
- [22] R.J. Nicholls, N. Ni, S. Lozano-Perez, A. London, D.W. McComb, P.D. Nellist, C. R. Grovenor, C.J. Pickard, J.R. Yates, Crystal structure of the ZrO phase at zirconium/zirconium oxide interfaces, *Adv. Eng. Mater.* 17 (2) (2015) 211–215.
- [23] B. Puchala, A. Van der Ven, Thermodynamics of the Zr-O system from first-principles calculations, *Phys. Rev. B* 88 (9) (2013) 094108.
- [24] Y. Ishii, J.M. Sykes, Microstructure of oxide layers formed on Zircaloy-2 in air at 450°C, *Mater. High Temp.* 17 (1) (2014) 23–28.
- [25] N. Ni, S. Lozano-Perez, J. Sykes, C. Grovenor, Quantitative EELS analysis of zirconium alloy metal/oxide interfaces, *Ultramicroscopy* 111 (2) (2011) 123–130.
- [26] J. Hu, A. Garner, N. Ni, A. Gholinia, R.J. Nicholls, S. Lozano-Perez, P. Frankel, M. Preuss, C.R. Grovenor, Identifying suboxide grains at the metal-oxide interface of a corroded Zr-1.0%Nb alloy using (S)TEM, transmission-EBSD and EELS, *Micron* 69 (2015) 35–42.
- [27] P. Bossis, G. Lelièvre, P. Barberis, X. Iltis, F. Lefebvre, Multi-scale characterization of the metal-oxide interface of zirconium alloys, in: G.D. Moan (Ed.), *Zirconium in the Nuclear Industry: Twelfth International Symposium*, ASTM International, West Conshohocken, PA, 2000, pp. 918–945.
- [28] X. Iltis, H. Michel, Caractérisation par microscopie électronique à transmission d’une solution solide Zr-O localement ordonnée obtenue à l’issue d’un traitement d’oxydation sur un alliage de type Zircaloy-4, *J. Alloy. Compd.* 177 (1) (1991) 71–82.
- [29] Y. Dong, A.T. Motta, E.A. Marquis, Atom probe tomography study of alloying element distributions in Zr alloys and their oxides, *J. Nucl. Mater.* 442 (1–3) (2013) 270–281.
- [30] B. de Gabory, Y. Dong, A.T. Motta, E.A. Marquis, EELS and atom probe tomography study of the evolution of the metal/oxide interface during zirconium alloy oxidation, *J. Nucl. Mater.* 462 (2015) 304–309.
- [31] G. Sundell, M. Thuvander, H.-O. Andrén, Barrier oxide chemistry and hydrogen pick-up mechanisms in zirconium alloys, *Corros. Sci.* 102 (2016) 490–502.
- [32] B. Wadman, Z. Lai, H.O. Andrén, A.L. Nyström, P. Rudling, H. Pettersson, Microstructure of oxide layers formed during autoclave testing of zirconium alloys, in: E.R. Bradley (Ed.), *Zirconium in the Nuclear Industry*, Tenth International Symposium, ASTM International, West Conshohocken, PA, 1994, pp. 579–598.
- [33] P. Tejlund, M. Thuvander, H.-O. Andrén, S. Ciurea, T. Andersson, M. Dahlbäck, L. Hallstadius, Detailed analysis of the microstructure of the metal/oxide interface region in zircaloy-2 after autoclave corrosion testing, *J. ASTM Int.* 8 (6) (2011) 1–16.
- [34] A. Garner, F. Baxter, P. Frankel, M. Topping, A. Harte, T. Slater, P. Tejlund, J.E. Romero, E.C. Darby, A. Cole-Baker, M. Gass, M. Preuss, Investigating the effect of zirconium oxide microstructure on corrosion performance: a comparison between neutron, proton, and nonirradiated oxides, *Zirconium in the Nuclear Industry: 18th International Symposium*, 2018, pp. 491–523.
- [35] D. Hudson, A. Cerezo, G.D.W. Smith, Zirconium oxidation on the atomic scale, *Ultramicroscopy* (2009) 667–671.
- [36] B. Cox, Some effects of pressure on the oxidation of zircaloy-2 in steam and oxygen, *J. Less Common Met.* 5 (4) (1963) 325–336.
- [37] J. Liu, K. Li, J. Sayers, T. Aarholt, G. He, H. Hulme, A. Garner, M. Preuss, H. Nordin, J.M. Partezana, M. Limbäck, S. Lozano-Perez, S. Ortner, C.R. M. Grovenor, Characterisation of deuterium distributions in corroded zirconium alloys using high-resolution SIMS imaging, *Acta Mater.* 200 (2020) 581–596.
- [38] E. Hillner, D.G. Franklin, J.D. Smee, Long-term corrosion of Zircaloy before and after irradiation, *J. Nucl. Mater.* 278 (2) (2000) 334–345.
- [39] J.S. Bryner, The cyclic nature of corrosion of zircaloy-4 in 633 K water, *J. Nucl. Mater.* 82 (1) (1979) 84–101.
- [40] D.H. Bradhurst, P.M. Heuer, The influence of oxide stress on the breakaway oxidation of zircaloy-2, *J. Nucl. Mater.* 37 (1) (1970) 35–47.
- [41] T. Ahmed, L.H. Keys, The breakaway oxidation of zirconium and its alloys a review, *J. Less Common Met.* 39 (1) (1975) 99–107.
- [42] A. Yilmazbayhan, E. Breval, A.T. Motta, R.J. Comstock, Transmission electron microscopy examination of oxide layers formed on Zr alloys, *J. Nucl. Mater.* 349 (3) (2006) 265–281.
- [43] B. Cox, Processes occurring during the breakdown of oxide films on zirconium alloys, *J. Nucl. Mater.* 29 (1) (1969) 50–66.
- [44] A. Rogerson, R.A. Murgatroyd, Breakaway growth in annealed Zircaloy-2 at 353 K and 553 K, *J. Nucl. Mater.* 113 (2) (1983) 256–259.
- [45] F. Garzarolli, H. Seidel, R. Tricot, J.P. Gros, Oxide growth mechanism on zirconium alloys, in: A.M. Garde (Ed.), *Zirconium in the Nuclear Industry: Ninth International Symposium*, ASTM International, West Conshohocken, PA, 1991, pp. 395–415.
- [46] H.J. Beie, A. Mitwalsky, F. Garzarolli, H. Ruhmann, H.J. Sell, Examinations of the corrosion mechanism of zirconium alloys, in: E.R. Bradley (Ed.), *Zirconium in the Nuclear Industry: Tenth International Symposium*, ASTM International, West Conshohocken, PA, 1994, pp. 615–643.
- [47] S. Abolhassani, A. Baris, R. Grabherr, J. Hawes, A. Coldeweih, R. Vanta, R. Restani, A. Hermann, J. Bertsch, M. Chollet, G. Kuri, M. Martin, S. Portier, H. Wiese, H. Schweikert, G. Bart, K. Ammon, G. Ledergerber, M. Limbäck, Toward an improved understanding of the mechanisms involved in the increased hydrogen uptake and corrosion at high burnups in zirconium based claddings, in: A.T. Motta, S.K. Yagnik (Eds.), *Zirconium in the Nuclear Industry: 19th International Symposium*, ASTM International, West Conshohocken, PA, 2021, pp. 435–466.
- [48] J. Hu, B. Setiadinata, T. Aarholt, A. Garner, A. Vilalta-Clemente, J.M. Partezana, P. Frankel, P. Bagot, S. Lozano-Perez, A. Wilkinson, M. Preuss, M. Moody, C. Grovenor, Understanding corrosion and hydrogen pickup of zirconium fuel cladding alloys: the role of oxide microstructure, porosity, suboxides, and second-phase particles, in: R.J. Comstock, A.T. Motta (Eds.), *Zirconium in the Nuclear Industry: 18th International Symposium*, ASTM International, West Conshohocken, PA, 2018, pp. 93–126.
- [49] A. Baris, Increased hydrogen uptake of zirconium based claddings at high burnup, *School of Metallurgy and Materials*, PhD thesis, University of Birmingham, 2019.
- [50] A. Baris, R. Restani, R. Grabherr, Y.L. Chiu, H.E. Evans, K. Ammon, M. Limbäck, S. Abolhassani, Chemical and microstructural characterization of a 9 cycle Zircaloy-2 cladding using EPMA and FIB tomography, *J. Nucl. Mater.* 504 (2018) 144–160.
- [51] M. Griffiths, R.W. Gilbert, G.J.C. Carpenter, Phase instability, decomposition and redistribution of intermetallic precipitates in Zircaloy-2 and -4 during neutron irradiation, *J. Nucl. Mater.* 150 (1) (1987) 53–66.

- [52] S. Valizadeh, G. Ledergerber, S. Abolhassan, D. Jädernäs, M. Dahlbäck, E. Mader, G. Zhou, J. Wright, L. Hallstadius, Effects of secondary phase particle dissolution on the in-reactor performance of BWR cladding, *J. ASTM Int.* 8 (2) (2011) 1–16.
- [53] G. Sundell, M. Thuvander, P. Tejländ, M. Dahlbäck, L. Hallstadius, H.O. Andrén, Redistribution of alloying elements in Zircaloy-2 after in-reactor exposure, *J. Nucl. Mater.* 454 (1-3) (2014) 178–185.
- [54] T. Sawabe, T. Sonoda, Evolution of nanoscopic iron clusters in irradiated zirconium alloys with different iron contents, *J. Nucl. Sci. Technol.* 55 (10) (2018) 1110–1118.
- [55] T. Sawabe, T. Sonoda, An atom probe study on the Fe distribution in Zr-based alloys with different Fe content under high fluence neutron irradiation, *J. Nucl. Mater.* 567 (2022) 153809.
- [56] J. Eriksson, D. Mayweg, G. Sundell, H.-O. Andrén, M. Thuvander, Solute concentrations in the matrix of zirconium alloys studied by atom probe tomography, in: K. Yagnik, M. Preuss (Eds.), *Zirconium in the Nuclear Industry: 20th International Symposium*, ASTM STP 1645, Ottawa, 2023, pp. 149–172.
- [57] J. Eriksson, G. Sundell, P. Tejländ, H.-O. Andrén, M. Thuvander, An atom probe tomography study of the chemistry of radiation-induced dislocation loops in Zircaloy-2 exposed to boiling water reactor operation, *J. Nucl. Mater.* 550 (2021) 152923.
- [58] J. Eriksson, G. Sundell, P. Tejländ, H.-O. Andrén, M. Thuvander, Nanoscale chemistry of Zircaloy-2 exposed to three and nine annual cycles of boiling water reactor operation — an atom probe tomography study, *J. Nucl. Mater.* 561 (2022) 153537.
- [59] A. Harte, D. Jädernäs, M. Topping, P. Frankel, C.P. Race, J. Romero, L. Hallstadius, E.C. Darby, M. Preuss, The effect of matrix chemistry on dislocation evolution in an irradiated Zr alloy, *Acta Mater.* 130 (2017) 69–82.
- [60] A. Harte, M. Topping, P. Frankel, D. Jädernäs, J. Romero, L. Hallstadius, E. C. Darby, M. Preuss, Nano-scale chemical evolution in a proton-and neutron-irradiated Zr alloy, *J. Nucl. Mater.* 487 (2017) 30–42.
- [61] B.C. Cheng, R.M. Kruger, R.B. Adamson, Corrosion behavior of irradiated zircaloy, in: A.M. Garde, E.R. Bradley (Eds.), *Zirconium in the Nuclear Industry: Tenth International Symposium*, ASTM International, West Conshohocken, PA, 1994, pp. 400–418.
- [62] Y. Takagawa, S. Ishimoto, Y. Etoh, T. Kubo, K. Ogata, O. Kubota, The correlation between microstructures and in-BWR corrosion behavior of highly irradiated Zr-based alloys, *J. ASTM Int.* 2 (1) (2005) JA112357.
- [63] A. Harte, A comparison of proton and neutron irradiation-induced microstructural and microchemical evolution in Zircaloy-2, PhD thesis, The University of Manchester, 2015.
- [64] Z. Yu, M. Bachhav, F. Teng, L. He, A. Couet, Nanoscale redistribution of alloying elements in high-burnup AXIOM-2 (X2®) and their effects on in-reactor corrosion, *Corros. Sci.* 190 (2021).
- [65] G. Sundell, M. Thuvander, H.-O. Andrén, Tin clustering and precipitation in the oxide during autoclave corrosion of Zircaloy-2, *J. Nucl. Mater.* 456 (2015) 409–414.
- [66] A. Baris, S. Abolhassani, R. Grabherr, R. Restani, R. Schäublin, Y.L. Chiu, H. E. Evans, K. Ammon, M. Limbäck, Causes of increased corrosion and hydrogen uptake of Zircaloy-2 cladding at high burnups – a comparative study of the chemical composition of a 3 cycle and a 9-cycle cladding, *TopFuel*, Prague, 2018.
- [67] F. Garzarolli, B. Cox, P. Rudling, Optimization of Zry-2 for high burnups, in: M. Limbäck, P. Barbéris (Eds.), *Zirconium in the Nuclear Industry: 16th International Symposium*, ASTM International, West Conshohocken, PA, 2010, pp. 711–728.
- [68] M. Lindgren, G. Sundell, I. Panas, L. Hallstadius, M. Thuvander, H.O. Andrén, Toward a comprehensive mechanistic understanding of hydrogen uptake in zirconium alloys by combining atom probe analysis with electronic structure calculations, in: R. Comstock, P. Barberis (Eds.), *Zirconium in the Nuclear Industry: 17th International Symposium*, STP 1543, 2015, pp. 515–539.
- [69] Y.R. Than, R.W. Grimes, B.D.C. Bell, M.R. Wenman, Understanding the role of Fe, Cr and Ni in Zircaloy-2 with special focus on the role of Ni on hydrogen pickup, *J. Nucl. Mater.* 530 (2020).
- [70] B. Gault, A. Chiramonti, O. Cojocar-Mirédin, P. Stender, R. Dubosq, C. Freysoldt, S.K. Makineni, T. Li, M. Moody, J.M. Cairney, Atom probe tomography, *Nat. Rev. Methods Prim.* 1 (1) (2021) 51.
- [71] A.J. Breen, I. Mouton, W. Lu, S. Wang, A. Szczepaniak, P. Kontis, L.T. Stephenson, Y. Chang, A.K. da Silva, C.H. Liebscher, D. Raabe, T.B. Britton, M. Herbig, B. Gault, Atomic scale analysis of grain boundary deuteride growth front in Zircaloy-4, *Scr. Mater.* 156 (2018) 42–46.
- [72] I. Mouton, A.J. Breen, S. Wang, Y. Chang, A. Szczepaniak, P. Kontis, L. T. Stephenson, D. Raabe, M. Herbig, T.B. Britton, B. Gault, Quantification challenges for atom probe tomography of hydrogen and deuterium in zircaloy-4, *Microsc. Microanal.* 25 (2) (2019) 481–488.
- [73] I. Mouton, Y. Chang, P. Chakraborty, S. Wang, L.T. Stephenson, T. Ben Britton, B. Gault, Hydride growth mechanism in zircaloy-4: investigation of the partitioning of alloying elements, *Materialia* 15 (2021) 101006 (Oxf).
- [74] B.M. Jenkins, J. Haley, M.P. Moody, J.M. Hyde, C.R.M. Grovenor, APT and TEM study of behaviour of alloying elements in neutron-irradiated zirconium-based alloys, *Scr. Mater.* 208 (2022) 114323.
- [75] ASTM B811–13, Standard specification for wrought zirconium alloy seamless tubes for nuclear reactor fuel cladding (2022), <https://doi.org/10.1520/b0811-13r22e01>.
- [76] J.M. Wright, M. Limbäck, D. Schrire, M. Owaki, M. Nilsson, Commercial introduction and experience with the advanced high iron cladding HIF1® in boiling water reactors, *TopFuel*, Prague, 2018.
- [77] D. Mayweg, J. Eriksson, O. Bäcke, A.J. Breen, M. Thuvander, Focused ion beam induced hydride formation does not affect Fe, Ni, Cr-clusters in irradiated Zircaloy-2, *J. Nucl. Mater.* 581 (2023) 154444.
- [78] D. Mayweg, J. Eriksson, M. Sattari, G. Sundell, M. Limbäck, I. Panas, H. O. Andrén, M. Thuvander, Formation of pure zirconium islands inside c-component loops in high-burnup fuel cladding, *J. Nucl. Mater.* (2024) 155116.
- [79] D. Mayweg, J. Eriksson, M. Sattari, M. Thuvander, Limits of hydrogen analysis by atom probe tomography targeting Zr(Fe,Cr)₂ second phase particles in Zr-based fuel cladding from reactor operation, *J. Nucl. Mater.* 601 (2024) 155343.
- [80] J. Eriksson, Evolution of microstructure and nanoscale chemistry of zircaloy-2-type alloys during nuclear reactor operation, in: PhD thesis, Department of Physics, Chalmers University of Technology, 2022.
- [81] L. Walters, S.R. Douglas, M. Griffiths, Equivalent Radiation Damage in Zirconium Irradiated in Various Reactors, in: R.J. Comstock, A.T. Motta (Eds.), *Zirconium in the Nuclear Industry*, ASTM International, West Conshohocken, PA, 2018, pp. 676–690.
- [82] K. Thompson, D. Lawrence, D.J. Larson, J.D. Olson, T.F. Kelly, B. Gorman, *In situ* site-specific specimen preparation for atom probe tomography, *Ultramicroscopy* 107 (2-3) (2007) 131–139.
- [83] S.M. Hanlon, S.Y. Persaud, F. Long, A. Korinek, M.R. Daymond, A solution to FIB induced artefact hydrides in Zr alloys, *J. Nucl. Mater.* 515 (2019) 122–134.
- [84] Y. Chang, W. Lu, J. Guenole, L.T. Stephenson, A. Szczepaniak, P. Kontis, A. K. Ackerman, F.F. Dear, I. Mouton, X. Zhong, S. Zhang, D. Dye, C.H. Liebscher, D. Ponge, S. Korte-Kerzel, D. Raabe, B. Gault, Ti and its alloys as examples of cryogenic focused ion beam milling of environmentally-sensitive materials, *Nat. Commun.* 10 (1) (2019) 942.
- [85] O.C. Hellman, J.A. Vandembroucke, J. Rüsing, D. Isheim, D.N. Seidman, Analysis of three-dimensional atom-probe data by the proximity histogram, *Microsc. Microanal.* 6 (5) (2000) 437–444.
- [86] D.R. Kingham, The post-ionization of field evaporated ions: a theoretical explanation of multiple charge states, *Surf. Sci.* 116 (2) (1982) 273–301.
- [87] M. Bachhav, G. Pawar, F. Vurpillot, R. Danoix, F. Danoix, B. Hannyer, Y. Dong, E. Marquis, Interpreting the presence of an additional oxide layer in analysis of metal oxides–metal interfaces in atom probe tomography, *J. Phys. Chem. C* 123 (2) (2018) 1313–1319.
- [88] L. Chen, B. Luan, S. Ma, P. Wan, G. Bai, Y. Liu, Y. Zhang, Discussion on the presence condition of suboxide ZrO beneath the oxide in zirconium alloys, *J. Nucl. Mater.* 571 (2022).
- [89] M.I. Isik, A. Kostka, V.A. Yardley, K.G. Pradeep, M.J. Duarte, P.P. Choi, D. Raabe, G. Eggeler, The nucleation of Mo-rich Laves phase particles adjacent to M23C6 micrograin boundary carbides in 12% Cr tempered martensite ferritic steels, *Acta Mater.* 90 (2015) 94–104.
- [90] S.C.H. Llewellyn, K.A. Christofidou, V.J. Araullo-Peters, N.G. Jones, M.C. Hardy, E.A. Marquis, H.J. Stone, The effect of Ni:Co ratio on the elemental phase partitioning in γ - γ' Ni-Co-Al-Ti-Cr alloys, *Acta Mater.* 131 (2017) 296–304.
- [91] S. Dasari, A. Sarkar, A. Sharma, B. Gwalani, D. Choudhuri, V. Soni, S. Manda, I. Samajdar, R. Banerjee, Recovery of cold-worked Al_{0.3}CoCrFeNi complex concentrated alloy through twinning assisted B2 precipitation, *Acta Mater.* 202 (2021) 448–462.
- [92] J.P. Abriata, J. Garcés, R. Versaci, The O–Zr (Oxygen-Zirconium) system, *Bull. Alloy Ph. Diagr.* 7 (2) (1986) 116–124.
- [93] B. Gault, M.P. Moody, J.M. Cairney, S.P. Ringer, *Atom Probe Microscopy*, Springer, New York, 2012.
- [94] M.K. Miller, M.G. Hetherington, Local magnification effects in the atom probe, *Surf. Sci.* 246 (1) (1991) 442–449.
- [95] G. Sundell, M. Thuvander, A.K. Yatim, H. Nordin, H.-O. Andrén, Direct observation of hydrogen and deuterium in oxide grain boundaries in corroded Zirconium alloys, *Corros. Sci.* 90 (2015) 1–4.
- [96] G. Sundell, M. Thuvander, H.-O. Andrén, Enrichment of Fe and Ni at metal and oxide grain boundaries in corroded Zircaloy-2, *Corros. Sci.* 65 (2012) 10–12.
- [97] P. Kontis, H.A.M. Yusof, S. Pedrazzini, M. Danaie, K.L. Moore, P.A.J. Bagot, M. P. Moody, C.R.M. Grovenor, R.C. Reed, On the effect of boron on grain boundary character in a new polycrystalline superalloy, *Acta Mater.* 103 (2016) 688–699.
- [98] A. Jostsons, P.M. Kelly, R.G. Blake, The nature of dislocation loops in neutron irradiated zirconium, *J. Nucl. Mater.* 66 (3) (1977) 236–256.
- [99] A. Jostsons, P. Kelly, R. Blake, K. Farrell, Neutron Irradiation-Induced Defect Structures in Zirconium, J.A. Sprague, D. Kramer (Eds.), in: *Effects of Radiation on Structural Materials*, ASTM STP 683, ASTM International, 1979, pp. 46–61.
- [100] S. Yagnik, R. Adamson, G. Kobyljansky, J.-H. Chen, D. Gilbon, S. Ishimoto, T. Fukuda, L. Hallstadius, A. Obukhov, S. Mahmood, Effect of alloying elements, cold work, and hydrogen on the irradiation-induced growth behavior of zirconium alloy variants, in: R.J. Comstock, A.T. Motta (Eds.), *Zirconium in the Nuclear Industry: 18th International Symposium*, ASTM International, West Conshohocken, PA, 2018, pp. 748–795.
- [101] P. Tejländ, H.-O. Andrén, Origin and effect of lateral cracks in oxide scales formed on zirconium alloys, *J. Nucl. Mater.* 430 (1-3) (2012) 64–71.
- [102] R.B. Adamson, Effects of neutron irradiation on microstructure and properties of zircaloy, in: G.D. Moan (Ed.), *Zirconium in the Nuclear Industry: Twelfth International Symposium*, ASTM International, West Conshohocken, PA, 2000, pp. 15–31.
- [103] G.M. Hood, Point defect diffusion in α -Zr, *J. Nucl. Mater.* 159 (1988) 149–175.
- [104] M. Christensen, W. Wolf, C.M. Freeman, E. Wimmer, R.B. Adamson, L. Hallstadius, P.E. Cantonwine, E.V. Mader, Effect of alloying elements on the properties of Zr and the Zr–H system, *J. Nucl. Mater.* 445 (1-3) (2014) 241–250.

- [105] P.A. Burr, M.R. Wenman, B. Gault, M.P. Moody, M. Ivermark, M.J.D. Rushton, M. Preuss, L. Edwards, R.W. Grimes, From solid solution to cluster formation of Fe and Cr in α -Zr, *J. Nucl. Mater.* 467 (2015) 320–331.
- [106] B.D.C. Bell, S.T. Murphy, P.A. Burr, R.W. Grimes, M.R. Wenman, Accommodation of tin in tetragonal ZrO₂, *J. Appl. Phys.* 117 (8) (2015).
- [107] K. Takeda, H. Anada, Mechanism of corrosion rate degradation due to tin, in: G. D. Moan (Ed.), *Zirconium in the Nuclear Industry: Twelfth International Symposium*, ASTM International, West Conshohocken, PA, 2000, pp. 592–608.
- [108] A. Garner, J. Hu, A. Harte, P. Frankel, C. Grovenor, S. Lozano-Perez, M. Preuss, The effect of Sn concentration on oxide texture and microstructure formation in zirconium alloys, *Acta Mater.* 99 (2015) 259–272.
- [109] S.S. Yardley, K.L. Moore, N. Ni, J.F. Wei, S. Lyon, M. Preuss, S. Lozano-Perez, C.R. M. Grovenor, An investigation of the oxidation behaviour of zirconium alloys using isotopic tracers and high resolution SIMS, *J. Nucl. Mater.* 443 (1-3) (2013) 436–443.
- [110] P. Tejland, H.-O. Andrén, G. Sundell, M. Thuvander, B. Josefsson, L. Hallstadius, M. Ivermark, M. Dahlbäck, Oxidation mechanism in zircaloy-2—the effect of SPP size distribution, in: B. Comstock, P. Barbéris (Eds.), *Zirconium in the Nuclear Industry: 17th Volume*, ASTM International, West Conshohocken, PA, 2015, pp. 1–31.
- [111] B. Gault, M.P. Moody, J.M. Cairney, S.P. Ringer, Atom probe crystallography, *Mater. Today* 15 (9) (2012) 378–386.
- [112] J.P. Pemsler, Diffusion of oxygen in zirconium and its relation to oxidation and corrosion, *J. Electrochem. Soc.* 105 (6) (1958) 315.
- [113] G.J.C. Carpenter, D.O. Northwood, The contribution of dislocation loops to radiation growth and creep of Zircaloy-2, *J. Nucl. Mater.* 56 (1975) 260–266.
- [114] R.A. Holt, R.W. Gilbert, V. Fidleris, Dislocation substructure in zirconium alloys irradiated in EBR-II, in: J.S. Perrin (Ed.), *Effects of Radiation on Materials*, ASTM International, West Conshohocken, PA, 1982, pp. 234–250.
- [115] M. Griffiths, J.F. Mecke, J.E. Winegar, Evolution of microstructure in zirconium alloys during irradiation, in: G.P. Sabol (Ed.), *Zirconium in the Nuclear Industry: Eleventh International Symposium*, ASTM International, West Conshohocken, PA, 1996, pp. 580–602.
- [116] B.A. Cheadle, C.E. Ells, W. Evans, The development of texture in zirconium alloy tubes, *J. Nucl. Mater.* 23 (2) (1967) 199–208.
- [117] S.J. Armson, A. Garner, F. Baxter, M.S. Yankova, C.P. Race, A. Cole-Baker, C. Riley, M. Preuss, P. Frankel, The importance of substrate grain orientation on local oxide texture and corrosion performance in α -Zr alloys, in: A.T. Motta, S. K. Yagnik (Eds.), *Zirconium in the Nuclear Industry: 19th International Symposium*, ASTM International, West Conshohocken, PA, 2021, pp. 878–903.
- [118] K. Kakiuchi, N. Itagaki, T. Furuya, A. Miyazaki, Y. Ishii, S. Suzuki, T. Terai, M. Yamawaki, Effect of iron on hydrogen absorption properties of zirconium alloys, *J. Phys. Chem. Solids* 66 (2) (2005) 308–311.
- [119] M. Lindgren, I. Panas, Impact of additives on zirconium oxidation by water: mechanistic insights from first principles, *RSC Adv.* 3 (44) (2013).
- [120] M. Lindgren, C. Geers, I. Panas, Possible origin and roles of nano-porosity in ZrO₂ scales for hydrogen pick-up in Zr alloys, *J. Nucl. Mater.* 492 (2017) 22–31.
- [121] J. Hu, J. Liu, S. Lozano-Perez, C.R.M. Grovenor, M. Christensen, W. Wolf, E. Wimmer, E.V. Mader, Hydrogen pickup during oxidation in aqueous environments: the role of nano-pores and nano-pipes in zirconium oxide films, *Acta Mater.* 180 (2019) 105–115.
- [122] P.A. Burr, S.T. Murphy, S.C. Lumley, M.R. Wenman, R.W. Grimes, Hydrogen accommodation in Zr second phase particles: implications for H pick-up and hydriding of Zircaloy-2 and Zircaloy-4, *Corros. Sci.* 69 (2013) 1–4.
- [123] C. Jones, V. Tuli, Z. Shah, M. Gass, P.A. Burr, M. Preuss, K.L. Moore, Evidence of hydrogen trapping at second phase particles in zirconium alloys, *Sci. Rep.* 11 (1) (2021) 4370.